Monthly Notices
of the
ROYAL ASTRONOMICAL SOCIETY

Mon. Not. R. Astron. Soc. **406,** 1409–1424 (2010) doi:10.1111/j.1365-2966.2010.16509.x

Evidence for episodic warm outflowing CO gas from the intermediate-mass young stellar object IRAS 08470–4321⋆

W.-F. Thi,[1]† E. F. van Dishoeck,[2,3] K. M. Pontoppidan[4] and E. Dartois[5]

[1]*SUPA, ‡ Institute for Astronomy, Royal Observatory Edinburgh, University of Edinburgh, Blackford Hill, Edinburgh EH9 3HJ*
[2]*Leiden Observatory, Leiden University, PO Box 9513, 2300, Leiden, the Netherlands*
[3]*Max Planck Institut für Extrarerrestrische Physics, Postfach 1312, 85741 Garching, Germany*
[4]*Division of Geological and Planetary Science, MS 150-21, California Institute of Technology, CA 91125, USA*
[5]*Astrochimie Expérimentale, Institut d'Astrophysique Spatiale, Université Paris-Sud, Bât. 121, F-91405 Orsay, France*

Accepted 2010 February 10. Received 2010 February 10; in original form 2009 September 30

ABSTRACT

We present a $R \simeq 10\,000$ M-band spectrum of LLN 19 (IRAS 08470−4321), a heavily embedded intermediate-mass young stellar object located in the Vela molecular cloud, obtained with the Very Large Telescope (VLT)-Infrared Spectrometer And Array Camera (ISAAC). The data were fitted by a two-slab cold-hot model and a wind model. The spectrum exhibits deep broad ro-vibrational absorption lines of ^{12}CO $v = 1 \leftarrow 0$ and ^{13}CO $v = 1 \leftarrow 0$. A weak CO ice feature at 4.67 μm is also detected. Differences in velocity indicate that the warm gas is distinct from the cold millimetre emitting gas, which may be associated with the absorption by cooler gas (45 K). The outflowing warm gas at 300–400 K and with a mass-loss rate varying between 0.48×10^{-7} and 4.2×10^{-7} $M_\odot$ yr^{-1} can explain most of the absorption. Several absorption lines were spectrally resolved in subsequent spectra obtained with the VLT-Cryogenic Infrared Echelle Spectrograph (CRIRES) instrument. Multiple absorption substructures in the high-resolution ($R = 100\,000$) spectra indicate that the mass-loss is episodic with at least two major events that occurred recently (<28 yr). The discrete mass-loss events together with the large turbulent width of the gas (dv = 10–12 km s^{-1}) are consistent with the predictions of the jet-bow shock outflow and the wide-angle wind model. The CO gas/solid column density ratio of 20–100 in the line of sight confirms that the circumstellar environment of LLN 19 is warm. We also derive a ^{12}C/^{13}C ratio of 67 ± 3, consistent with previous measurements in local molecular clouds but not with the higher ratios found in the envelope of other young stellar objects.

Key words: ISM: jets and outflows – ISM: lines and bands.

1 INTRODUCTION

The gas dynamics of the inner surroundings of low- and high-mass young stellar objects (YSOs) is a complex interplay between accretion, settling and ejection (e.g. Stahler & Palla 2005; Arce et al. 2007). The gas and dust of the collapsing envelope are accreting on to the YSOs or settling on to discs in Keplerian rotation. Meanwhile, powerful jets and winds remove the excess angular momentum dispersing the envelope and allowing the system to contract. The release of gravitational energy and the radiation of the YSOs heat the inner circumstellar gas to a few hundred to a few thousand kelvin. Mid-infrared observations best probe these regions for two reasons. First, dust grains absorb and scatter less in the infrared than in the visible. Secondly, atoms and molecules at a few hundred kelvin emit preferably in the mid-infrared.

Molecular ro-vibrational transitions trace the large range in density, temperature and ultraviolet radiation field encountered in circumstellar discs and envelopes. While rotational lines in the millimetre wavelength range trace the cool outer disc and envelope ($T <$ 100 K), the mid-infrared fundamental emission ($v = 1 \rightarrow 0$) and absorption ($v = 1 \leftarrow 0$) probe the warm part (T = 100–900 K) and the overtone emissions ($\Delta v = 2$) in the near-infrared the hot dust free region at $T >$ 1500 K (Bik & Thi 2004; Thi et al. 2005). CO ro-vibrational lines seen in absorption against the continuum generated by warm dust can probe cold as well as warm gases along the line of sight.

Fundamental absorption lines of CO, the second most abundant molecule after H_2, are detected in high-mass YSOs (e.g. Scoville et al. 1983; Mitchell et al. 1990). The line profiles indicate the

⋆Based on observations collected at the VLT of the European Southern Observatory (ESO) at La Silla and Paranal, Chile (ESO Programmes I64.I-0605 and I79.C-0151).

†E-mail: thiw@ujf-grenoble.fr
‡Scottish Universities Physics Alliances.

presence of quiescent cold gas located in the envelope as well as outflowing warm gases. Ro-vibrational CO gas lines in emission and in absorption have also been seen in the envelope (e.g. Boogert, Hogerheijde & Blake 2002a; Pontoppidan et al. 2002, 2003; Brittain et al. 2007) or in the inner disc (Lahuis et al. 2006) of low-mass embedded YSOs. Besides CO, absorption lines of formaldehyde (Roueff et al. 2006), C_2H_2, HCN, OCS, NH_3 (Evans, Lacy & Carr 1991), $^{13}C^{12}CH_2$, CH_3, NH_3, HNCO, CS (Knez et al. 2009) and methane (Boogert, Blake & Öberg 2004) are observed towards high-mass YSOs with high-dispersion spectrometers from the ground.

In this paper, we present an analysis of the CO fundamental absorption lines towards LLN 19 (IRAS 08470−4321), an intermediate-mass YSO located in the Vela molecular cloud D at an estimated distance of 700 pc (Liseau et al. 1992). The luminosity of the object ($L_* = 1600$ L$_\odot$) corresponds to a ∼6–7 M$_\odot$ protostar (Palla & Stahler 1993). LLN 19 is a deeply embedded ($A_V \sim 45$ mag) YSO with moderate water and CO ice abundance in its line of sight (Thi et al. 2006). Millimetre continuum emission shows that LLN 19 is surrounded by 3.5 M$_\odot$ of gas and dust in a 24-arcsec beam. Part of this matter likely forms a disc and the rest remains in the envelope (Massi et al. 1999). A molecular outflow is detected in the ^{12}CO $J = 1 \rightarrow 0$, C^{17}O $J = 1 \rightarrow 0$ and CS $J = 2 \rightarrow 1$ maps of LLN 19 (Wouterloot & Brand 1999). The total mass of the outflow reaches 55 M$_\odot$ if a kinematic distance of 2.24 kpc is adopted (Wouterloot & Brand 1999). Lorenzetti et al. (2002) found shocked H_2 emission around LLN 19 but could not definitively show that LLN 19 is the source of the outflow. Observation evidence for the episodic nature of large-scale molecular outflows is mounting in low- and high-mass YSOs (e.g. Arce & Goodman 2001). However, evidence for episodic warm inner winds exists primarily for high-mass YSOs from CO absorption studies (e.g. Mitchell, Maillard & Hasegawa 1991). Our work extends the study of inner warm winds to lower luminosity objects.

We describe the observation and data reduction procedures in Section 2 and give a first analysis of the results in Section 3. We analyse the data using a wind model for the Infrared Spectrometer And Array Camera (ISAAC) data and a wind-envelope model for the Cryogenic Infrared Echelle Spectrograph (CRIRES) data in Section 5 and Section 6, and discuss the implications of our analysis on the gas and ice content in the environment of LLN 19 in Section 7. Finally, we conclude in Section 8.

2 OBSERVATION AND DATA REDUCTION

We observed LLN 19 (IRAS 08470−4321) at a spectral resolving power of $R \approx 10\,000$ (resolution of 30 km s^{-1}) by setting the slit width to 0.3 arcsec with the ISAAC mounted on the Very Large Telescope-UT1 (VLT-UT1) as one of the targets of a ESO large programme to study the ice and gas around YSOs (van Dishoeck et al. 2003). The slit width corresponds to a physical distance of 210 au at the distance of LLN 19 (700 pc). We adopted the distance of 700 pc derived by Liseau et al. (1992) over the kinematic distance of 2.24 kpc. The closer distance is consistent with the YSO LLN 19 being a member of the Vela molecular cloud. We obtained an *M*-band spectrum from 4.5 to 4.8 μm of LLN 19. We also observed standard stars at same airmass with the same instrument settings. We restrict our analysis to the 4.55–4.8 μm region because the signal-to-noise ratio (S/N) is too low, below 4.55 μm, due to strong atmospheric CO_2 absorption. The detector for 3–5 μm observations is a 1024 × 1024 Aladdin InSb array. We reduced the data using an in-house software written in the Interactive Data Language (IDL) . The data reduction procedure is standard for infrared observations (bad pixel maps, flat fielding, distortion correction, etc.). Because of the scarcity of halogen lamp lines in the *M*-band, the spectrum was wavelength-calibrated by comparing the strong atmospheric absorption lines with high S/N spectra of the atmosphere above Paranal, measured by the ESO staff. The uncertainties in transmission are dominated by systematics from the telluric line removal procedure (Pontoppidan & van Dishoeck 2005). The precision of the wavelength calibration is ∼5 km s^{-1}, i.e. one-sixth of the resolution dv = 30 km s^{-1}, over the entire spectrum. Details on the data reduction procedures are described in Pontoppidan et al. (2003). At the time of the observation (2001 July 1), $v_{obs} = v_{LSR}$(LLN 19)+4.2 km s^{-1}.

Subsequent high-resolution observations at $R = 100\,000$ (dv = 3 km s^{-1}) of LLN 19 were obtained with the CRIRES at the VLT on 2007 April 26. CRIRES provides a resolving power of up to 10^5 in the spectral range from 1 to 5 μm when used with a 0.2-arcsec slit. The simultaneous spectral coverage between 4.64 and 4.85 μm was achieved using a mosaic of four Aladdin III InSb arrays, which combine into an effective 4096 × 512 focal-plane detector array in the focal plane. We used the adaptive optics (AO) system multi-applications curvature adaptive optics (MACAO) to optimize the S/N and the spatial resolution. In our observation, the S/N reaches ∼180. As for the ISAAC observations, chopping and nodding were used along the slit and standard stars were observed at the same airmass to correct for telluric absorption lines. The CRIRES data were reduced using standard procedures that includes flat-field correction, detector non-linearity correction and linearization of the spectra in both the dispersion- and cross-dispersion directions. We used a telluric model to wavelength-calibrate the spectrum and to blank out the telluric absorptions after division by the standard. The width of the continuum is 0.35 arcsec, consistent with the AO-corrected spatial resolution. The CRIRES data are part of a large programme that observed ∼100 YSOs and protoplanetary discs (Pontoppidan et al. 2008). A handful of the observed YSOs show high-velocity CO absorption features that can be ascribed to winds. In particular, the spectrum of LLN 19 has the deepest CO absorption features.

3 OBSERVATIONAL RESULTS

The continuum-subtracted ISAAC spectrum in Fig. 1 is dominated by deep gas phase ^{12}CO ro-vibrational $v = 1 \leftarrow 0$ *R*-branch ($J + 1 \leftarrow$, $J' = J + 1$, $J'' = J$) and *P*-branch ($J + 1 \rightarrow J$) absorption lines. A shallow absorption feature due to solid CO is also present in the spectrum.

^{12}CO *R*(0) and *R*(1), and *P*-branch transitions from one to 13 have been observed with CRIRES and a sample of those absorption lines is shown in Fig. 2. The absorption lines show multiple substructures, which correspond to the blue-wing absorption seen in the lower resolution ISAAC spectrum (Fig. 3). Such data are available only for the lower *J* lines, probing the cooler gas.

3.1 CO ice feature

A weak feature centred around 4.675 μm (2140 cm^{-1}) corresponding to CO ice is detected. The total solid CO column density is $(4.3 \pm 0.6) \times 10^{16}$ cm^{-2} using the band strength of A(CO) = 1.1 × 10^{-17} cm mol^{-1} at 14 K (Jiang, Person & Brown 1975; Schmitt, Greenberg & Grim 1989; Gerakines et al. 1995) to convert the integrated absorption to column density. The detailed analysis of the CO ice components in relation to other YSOs in the Vela cloud is provided by Thi et al. (2006).

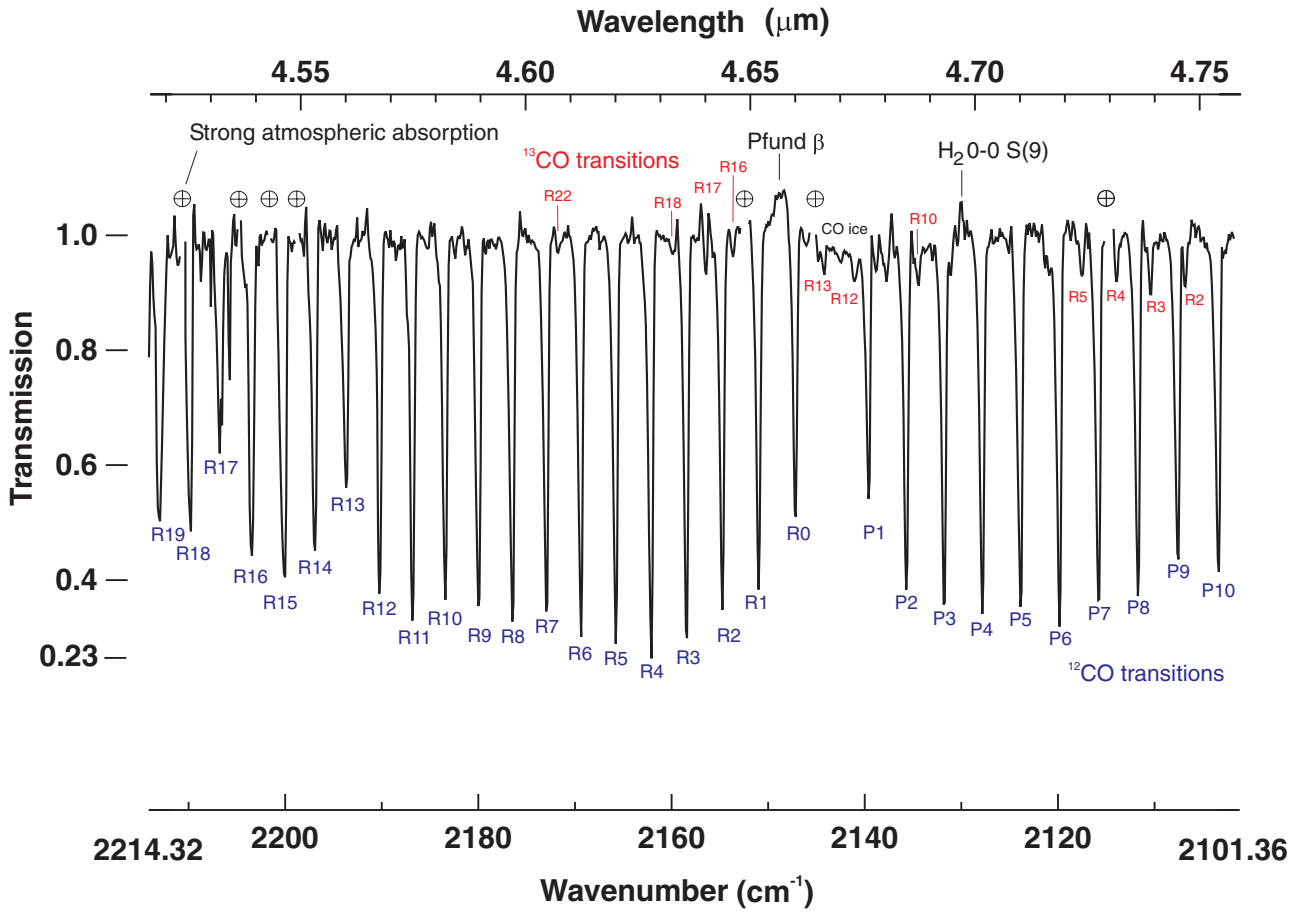

Figure 1. VLT-ISAAC *M*-band spectrum of LLN 19. The positions of the ^{12}CO and ^{13}CO lines are labelled. Wavelength regions with poor atmospheric transmission are omitted and labelled with a ⊕ symbol.

3.2 Gaseous components

3.2.1 ISAAC data

We first focus on the ISAAC spectrum. The LLN 19 spectrum is particularly rich in gas-phase lines. We detect the hydrogen-recombination emission line Pfβ, which is an indicator of accretion/wind activity and dense gases ($n_e \sim 10^8$ cm^{-3}), at 4.653 μm. The broad wings ($\Delta V = 300$–500 km s^{-1}) of the line can be ascribed to a stellar/disc wind, especially in low- and intermediate-mass stars surrounded by discs (e.g. Carmona et al. 2005). For high-mass stars, the stellar wind is driven by radiative pressure exerted on the ionic lines. We tentatively detect the pure rotational H_2 $0-0\,S(9)$ line at 4.695 μm with an equivalent width of $(27 \pm 12) \times 10^{-3}$ cm^{-1} (1σ). The line is also seen in the CRIRES data (see the lower right-hand panel of Fig. 2) with an equivalent width (EW) of $(11.4 \pm 3.5) \times 10^{-3}$ cm^{-1}. The detection of the H_2 line in emission, whose energy level lies at 5005.73 K, testifies the presence of hot molecular gas.

^{12}CO *R*- and *P*-branch lines, up to $J = 10$ and 19, respectively, are clearly seen (Fig. 1). The lines are up to 60 per cent deep at the spectral resolution of 30 km s^{-1}. Columns 2 and 3 of Table 1 contain the rest laboratory and observed wavenumbers. The quiescent cold gas around LLN 19 is located at v_{LSR}(mm) = 12 km s^{-1} from millimetre observations of ^{12}CO $J = 1 \rightarrow 0$ in a 46-arcsec beam (Wouterloot & Brand 1999). By contrast, the CO gas seen in the mid-infrared is moving by an average $v_{LSR} = -25$ km s^{-1} (± 5 km s^{-1}). The line velocities are not randomly scattered around the average-velocity shift value. The low-*J* lines have line widths smaller than the high-*J* lines, suggesting that quiescent cold gas may also be present in the line of sight, but the spectral resolution is too low to resolve it from the outflowing gas. The line profiles are not symmetric and can be decomposed into two Gaussian components: a deep component centred at $v_{LSR} = -25 \mp 5$ km s^{-1} with full width at half-maximum (FWHM) = 33 km s^{-1} and a broad shallower component at $v_{LSR} = -75 \mp 5$ km s^{-1} with FWHM = 59 km s^{-1}. Fig. 3 displays a normalized absorption line profile averaged over all the lines and its decomposition into the two components. The lines do not broaden with increasing quantum rotational number for the transition. The decomposition is arbitrary but allows a simple analysis of the two components.

In the rest of the paper, we will refer to the main (at -25 km s^{-1}) and blue (at -75 km s^{-1}) components. At the resolution of ∼30 km s^{-1}, the main and blue CO absorption lines are marginally resolved; the depth of the absorption lines indicates that the intrinsic width Δv is $\sim \sqrt{(\mathrm{FWHM})^2 - (\mathrm{Resolution})^2} = \sqrt{33^2 - 30^2} = 13.7$ km s^{-1} if the main absorption profile is caused by a single component. High-velocity blueshifted gas is commonly found towards high-mass (Mitchell et al. 1991) and low-mass YSOs (e.g. Lahuis et al. 2006).

Weaker ^{13}CO *R*-branch absorption lines are detected up to $J = 22$ as well and are labelled in Fig. 1. The blue part of the average

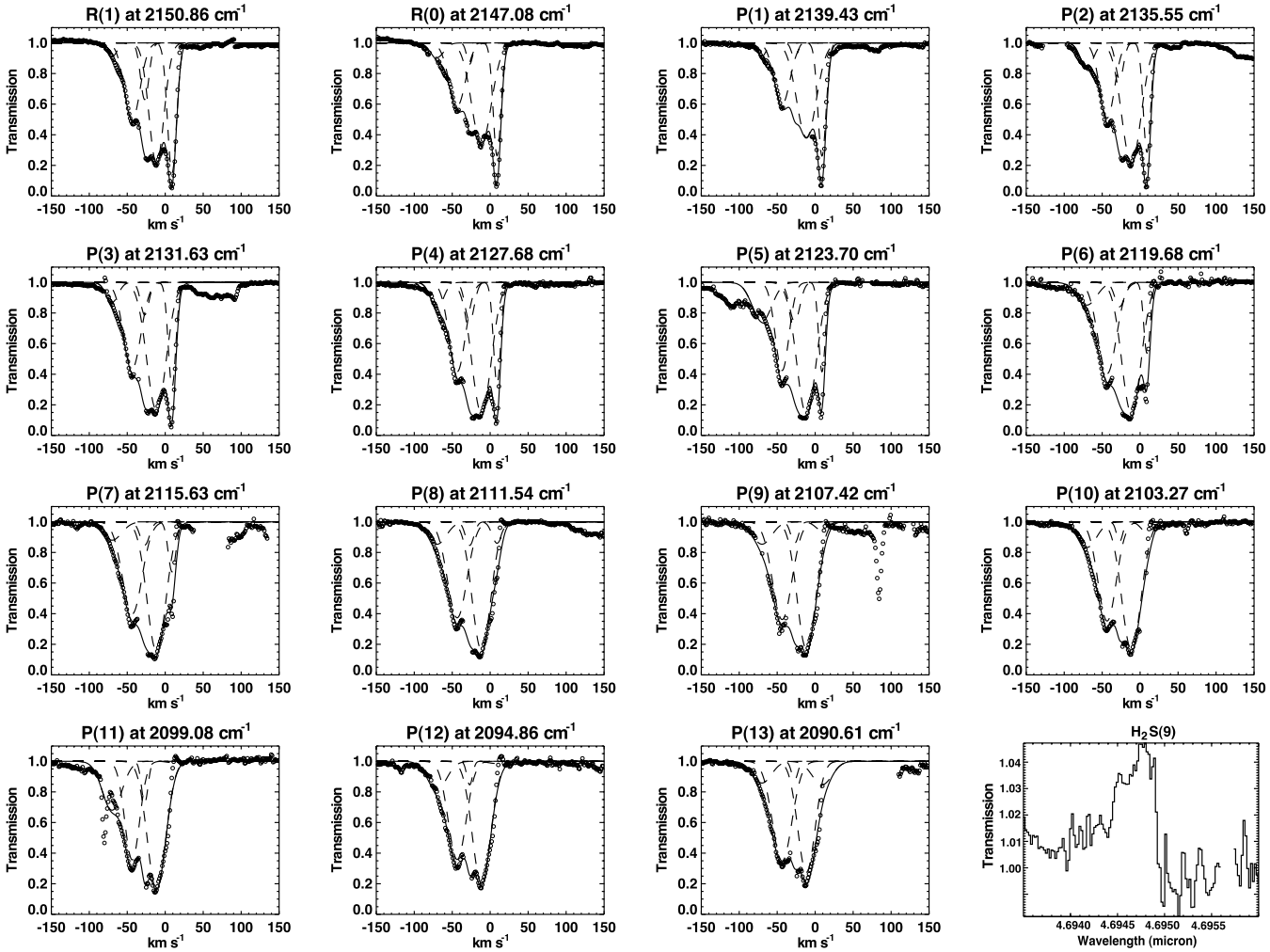

Figure 2. Absorption lines in open circles towards LLN 19, observed with VLT-CRIRES at a resolution of 3 km s^{-1}. Wavelength regions with poor atmospheric transmission are omitted. The long-dashed lines are the substructure fits and the continuous lines are the total fits, which are the sum of all the Gaussian sub-components.The lower right-hand panel shows the tentatively detected H_2 $S(9)$ line at 4.6947 μm by VLT-CRIRES.

^{13}CO profile is contaminated by other features, mostly by the wings of the ^{12}CO feature. The ^{13}CO lines are seen at the same velocity than their ^{12}CO counterpart. However, the weakness of the ^{13}CO lines forbids an accurate determination of the shifts.

The EWs of the main and blue component are given in Tables 1 and 2. The normalized EW ratios $W_{\tilde{\nu}}/\tilde{\nu} = W_\lambda/\lambda$ between ^{12}CO and ^{13}CO lines increase with increasing rotational quantum number but remain much lower than the interstellar isotopic value of $^{12}C/^{13}C =$ 60–65, suggesting that the ^{12}CO lines are optically thick.

3.2.2 CRIRES data

The CRIRES spectra show that the two components seen in the ISAAC spectrum actually consist of the absorption by four clumps at 9, −11.5, −27, −43.5 and −70 km s^{-1}. The components at 9, −11.5 and −27 km s^{-1} correspond to the main component in the ISAAC data while the −43.5 and −70 km s^{-1} components correspond to the blue wing. The absorption at 9 km s^{-1} may be saturated at the resolution of 3 km s^{-1}. As a result, the measured widths of the 9 km s^{-1} feature may be broader than the intrinsic widths.

We modelled the absorption lines by a combination of four Gaussians with fixed velocities v_i (9, −11.5, −27, −43.5 and −70 km s^{-1}). We performed our Gaussian decomposition in the transmission domain since we are interested in the EWs of each component. The fitting function has the form:

$$f(v) = 1 - \sum_i A_i \exp\left[-\left(\frac{v - v_i}{\delta v_i}\right)^2\right], \quad (1)$$

where A_i and δv_i, the widths and amplitudes of the Gaussians, are found by the fitting routine. The widths and amplitudes of the Gaussians are free parameters of the fits. We used the shuffled complex evolution (SCE) optimization code (see Section 5.1) to determine the best fits. The fit for each individual line is shown in Fig. 2, whereas the FWHM of the Gaussians and the EWs are shown in Fig. 4.

The largest EWs ($EW > 0.1$ cm^{-1}) correspond to the outflowing component at −11 km s^{-1}. The quiescent envelope component at 9 km s^{-1} shows decreasing EWs with increasing J values, testifying of a cold component. The large EW for $P(13)$ in the CRIRES data for the component at 9 km s^{-1} is most likely an artefact caused by missing data. The gas EWs do not show similar clear trend with increasing J values.

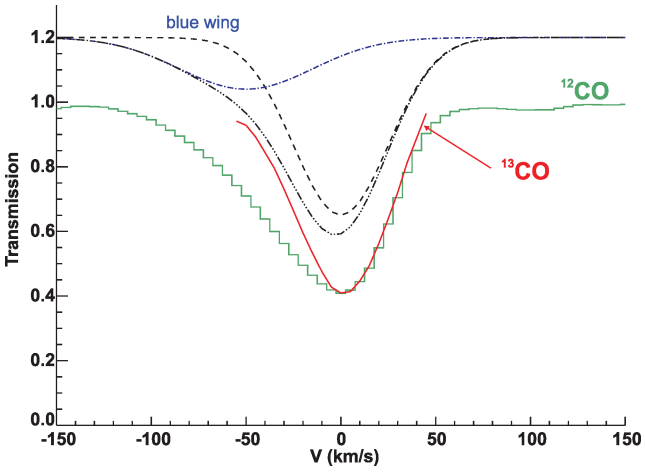

Figure 3. Comparison of the ^{12}CO and ^{13}CO average ISAAC profiles. The profiles are averages of all the detected lines to increase the S/N. The profiles are corrected for the Earth velocity at the day of the observation and are normalized to an absorption depth of 0.4 to ease the comparison. The model decompositions are shifted by +0.2 for clarity. Both mean profiles were shifted by $-9\,\mathrm{km\,s^{-1}}$.

The average FWHM of the Gaussians is consistent with an intrinsic turbulent width of $\sim$13.7 km s^{-1}, inferred from the ISAAC data. The parameters will be analysed in the following sections.

3.2.3 *Comparison between ISAAC and CRIRES data*

The measured EWs derived from ISAAC and CRIRES data are compared in Fig. 5. Discrepancies are small for most transitions (<15 per cent) except for $P(1)$ and $R(0)$. Generally the CRIRES EWs are larger than the ISAAC EWs. The lower resolution ISAAC data may suffer from systematic errors in the determination of the continuum, especially when the ^{12}CO blue-wing absorptions reach the wavelengths of the ^{13}CO absorption. The large differences for $P(1)$ and $R(0)$ may stem from the incomplete profiles in the CRIRES data set at those transitions due to strong telluric absorptions. In case of strong telluric absorptions, the data are interpolated to compensate for the missing data for the determination of the EW and this procedure can introduce significant systematic errors; in our case, an overestimate of the actual absorption (see Fig. 2). Strong telluric absorption features also introduce errors in the ISAAC EWs since the raw ISAAC data are ratioed by a standard star (Pontoppidan & van Dishoeck 2005). Alternatively, the choices made in the fitting of the CO ice absorption feature affect the continuum flux around the $P(1)$ and $R(0)$ lines, more strongly in the ISAAC spectrum than in the CRIRES spectrum (see Fig. 1). Therefore, the $P(1)$ and $R(0)$ EWs measured by ISAAC may be underestimated. In summary, the differences in EW between the two data sets can probably be ascribed to systematic errors in interpolating missing data and in cancelling telluric absorptions.

4 EQUIVALENT WIDTH ANALYSIS OF THE MAIN COMPONENT USING ISAAC DATA

4.1 Curve-of-growth analysis

We performed a classical curve-of-growth analysis of the ISAAC data, which relates the measured EW $W_{\tilde{\nu}}$ (in cm^{-1}) at wavenumber $\tilde{\nu}$ (in cm^{-1}) to the CO column density $N_{J''}$ (in cm^{-2}) in the initial lower rotational state J'' assuming a Gaussian profile with an intrinsic line width called the Doppler parameter $b_{\mathrm{D}} = \Delta v_{\mathrm{FWHM}}/2\log(2)^{1/2}$, where Δv_{FWHM} is the FWHM in km s^{-1} (e.g. Spitzer 1978, equation 3.22), and a slab geometry. We will focus on the ISAAC main component. The EWs, $W_{\tilde{\nu}}$ and $N_{J''}$, are linearly proportional only in the optically thin regime:

$$\frac{W_{\tilde{\nu}}}{\tilde{\nu}} = \left(1 - \frac{S_{J''}}{I_v^B}\right) \frac{\pi e^2}{m_e c^2} \frac{f_{J'\leftarrow J''} N_{J''}}{\tilde{\nu}}, \qquad (2)$$

Table 1. ^{12}CO $v = 1 \leftarrow 0$ R- and P-branch line positions and EWs of the middle component (mc) and blue component (bc) towards LLN 19.

Line	$\tilde{\nu}_{\mathrm{lab}}$ (cm^{-1})	$\tilde{\nu}_{\mathrm{obs}}$(mc) (cm^{-1})	$W_{\tilde{\nu}}$(mc) (10^{-3} cm^{-1})	$W_{\tilde{\nu}}$(bc) (10^{-3} cm^{-1})
$R(0)$	2147.081	2147.19	208.3 ± 1.6[a]	61.4 ± 0.3
$R(1)$	2150.856	2150.96	263.4 ± 14.3	77.7 ± 3.0
$R(2)$	2154.596	2154.72	279.7 ± 10.9	82.3 ± 2.3
$R(3)$	2158.300	2158.43	300.5 ± 2.5	88.7 ± 0.5
$R(4)$	2161.969	2162.07	306.9 ± 0.5	139.9 ± 0.2
$R(5)$	2165.601	2165.74	296.8 ± 0.7	135.2 ± 0.2
$R(6)$	2169.198	2169.34	292.5 ± 6.9	133.3 ± 2.3
$R(7)$	2172.759	2172.87	273.5 ± 5.2	145.9 ± 2.0
$R(8)$	2176.284	2176.42	281.3 ± 7.3	171.4 ± 3.2
$R(9)$	2179.772	2179.93	279.4 ± 8.9	123.6 ± 2.8
$R(10)$	2183.274	2183.38	275.6 ± 4.8	81.1 ± 1.0
$R(11)$	2186.639	2186.84	291.9 ± 6.3	85.9 ± 1.3
$R(12)$	2190.010	2190.24	271.9 ± 1.2	80.0 ± 0.3
$R(13)$	2193.359	2193.66	192.0 ± 1.2	70.6 ± 0.3
$R(14)$	2196.664	2196.88	239.8 ± 1.0	70.6 ± 0.2
$R(15)$	2199.931	2200.03	232.4 ± 3.9	191.6 ± 2.3
$R(16)$	2203.161	2203.42	231.6 ± 5.3	107.9 ± 1.8
$R(17)$	2206.354	2206.53	137.5 ± 27.4	149.5 ± 21.3
$R(18)$	2209.509	2209.80	213.9 ± 21.4	133.2 ± 9.5
$R(19)$	2212.626	2212.94	218.9 ± 31.9	96.6 ± 10.1
$P(1)$	2139.426	2139.59	182.0 ± 9.6	53.7 ± 2.0
$P(2)$	2135.546	2135.77	255.3 ± 1.9	75.3 ± 0.4
$P(3)$	2131.632	2131.74	272.3 ± 1.3	87.5 ± 0.3
$P(4)$	2127.684	2127.84	277.8 ± 3.5	102.4 ± 0.9
$P(5)$	2123.699	2123.86	278.4 ± 1.8	108.6 ± 0.5
$P(6)$	2119.681	2119.86	286.9 ± 2.5	135.4 ± 0.8
$P(7)$	2115.629	2115.78	267.3 ± 2.1	138.0 ± 0.8
$P(8)$	2111.543	2111.71	255.7 ± 12.0	124.6 ± 4.2
$P(9)$	2107.424	2107.57	229.7 ± 6.7	105.0 ± 2.2
$P(10)$	2103.270	2103.40	238.1 ± 3.7	108.8 ± 1.2

[a] 3σ fitting error.

Table 2. ^{13}CO $v = 1 \leftarrow 0$ R-branch line positions and EWs towards LLN 19.

Line	$\tilde{\nu}_{\mathrm{lab}}$ (cm^{-1})	$\tilde{\nu}_{\mathrm{obs}}$(mc) (cm^{-1})	$W_{\tilde{\nu}}$(mc) (10^{-3} cm^{-1})	$W_{\tilde{\nu}}$(bc)
$R(2)$	2106.903	2106.82	42.5 ± 4.5[a]	<5.9
$R(3)$	2110.447	2110.42	48.5 ± 4.5	–
$R(4)$	2113.958	2113.85	39.0 ± 4.5	∼9.6
$R(5)$	2117.436	2117.57	34.4 ± 4.5	–
$R(10)$	2134.318	2134.38	27.4 ± 4.5	∼21.7
$R(12)$	2140.833	2141.05	21.3 ± 4.5	–
$R(13)$	2144.039	2144.15	19.9 ± 4.5	–
$R(16)$	2153.447	2153.59	19.7 ± 4.5	–
$R(17)$	2156.514	2156.45	22.4 ± 4.5	–
$R(18)$	2159.545	2159.83	17.7 ± 4.5	–
$R(22)$	2171.317	2171.75	16.4 ± 4.5	–

[a] Formal 3σ error dominated by the flux calibration accuracy.

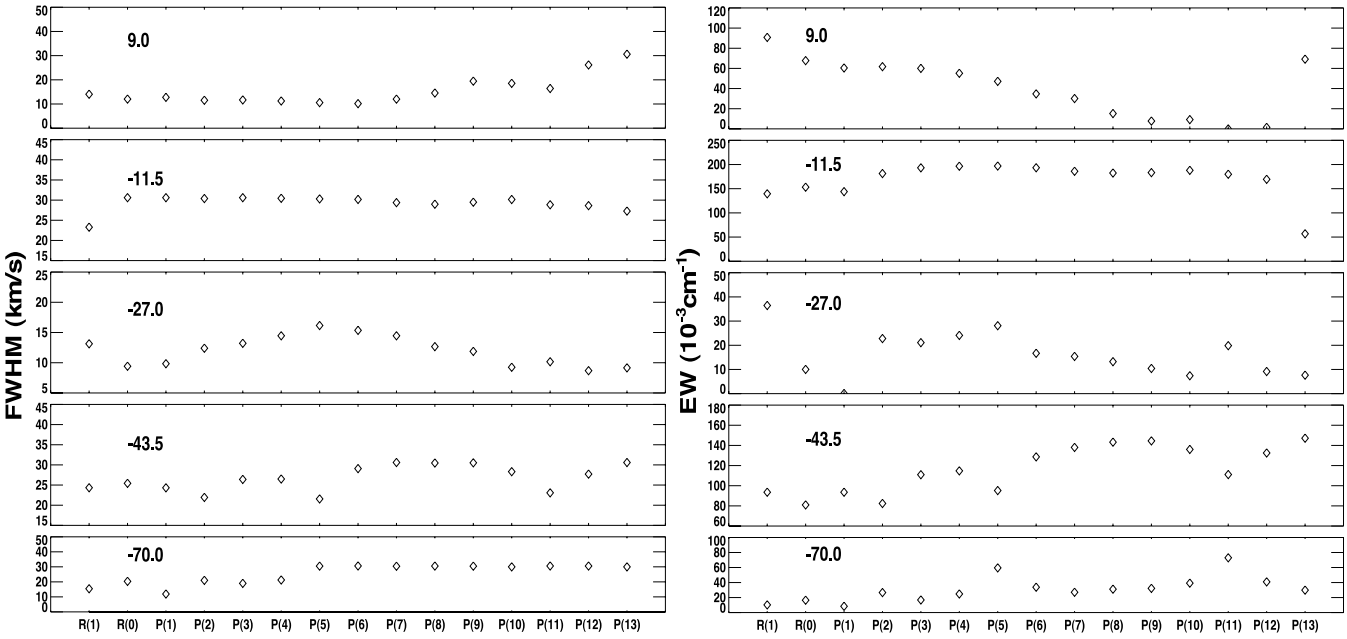

Figure 4. Gaussian width (left-hand panel) and EW (right-hand panel) for each individual substructure and each transition (x-axis) for the CRIRES. The number in each panel indicates the velocity of the substructures. The main causes of uncertainties are missing data due to strong telluric absorptions.

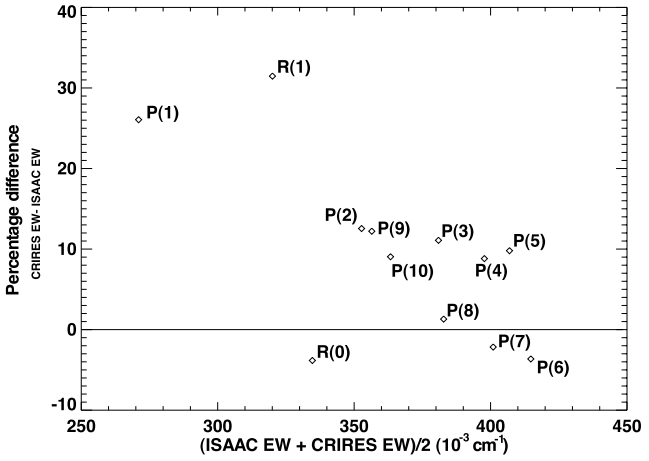

Figure 5. Plot of percentage difference versus mean value between EWs derived from the ISAAC and the CRIRES observations. The systematic differences are below 20 per cent except for the $P(1)$ and $R(1)$ transitions ($\sim$30 per cent).

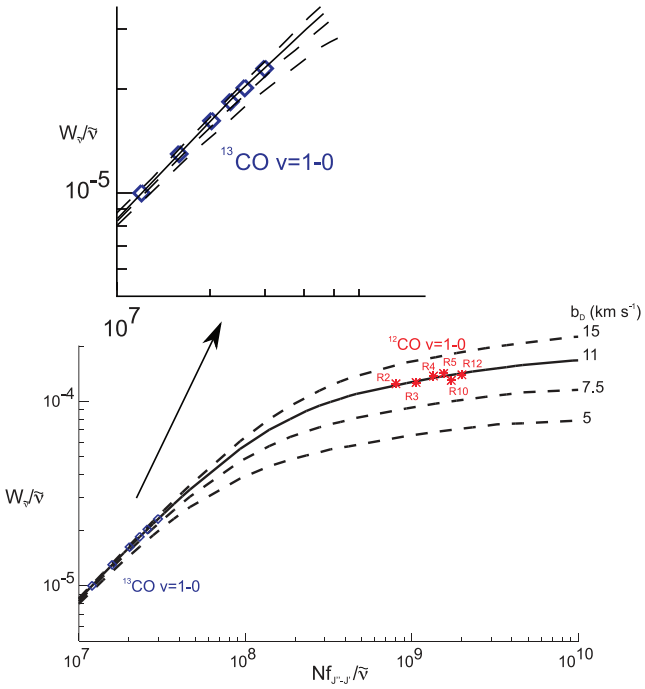

Figure 6. Curve of growth. Only the ^{12}CO EWs are affected by saturation and thus can be used to constrain the Doppler parameter b_D. The ^{13}CO EWs are on the linear part of the curve. The fits for the ^{13}CO EW are also shown in the inset for better clarity. The best-fitting curve to the data is obtained with $b_D = 11 \pm 1.5\,\mathrm{km\,s^{-1}}$ and $^{12}C/^{13}C = 67 \pm 3$.

where $f_{J'\leftarrow J''}$ is the oscillator strength (dimensionless) of the transition (Goorvitch & Chackerian 1994), I_ν^B is the background intensity and $S_{J''}$ is the transition source function in the extended region covered by the beam and the other symbols have their usual meaning. We assume here that $S_{J''}/I_\nu^B \ll 1$. Therefore, the derived column densities are lower limits to the actual values.

Transitions that were detected in both ^{12}CO and ^{13}CO with good S/N in the ISAAC data are shown in Fig. 6. The vertical axis corresponds to the observed $W_\tilde{\nu}/\tilde{\nu}$, while the horizontal axis corresponds to the different values of $N_{J''}(^{13}\mathrm{CO})f_{J'\leftarrow J''}(^{13}\mathrm{CO})/\tilde{\nu}$ and $N_{J''}(^{12}\mathrm{CO})f_{J'\leftarrow J''}(^{12}\mathrm{CO})/\tilde{\nu}$. Theoretical curve of growths computed assuming various values for the Doppler parameter b_D are overplotted in dashed lines. The column density in a given level J'' is computed by the equation

$$N_{J''}(^{13}\mathrm{CO}) = \frac{b_D \tau(^{13}\mathrm{CO})\tilde{\nu}}{1.497 \times 10^{-2} f_{J'\leftarrow J''}}. \quad (3)$$

Once the $\tau(^{13}\mathrm{CO})$ values are derived from the relationship between τ and $W_\tilde{\nu}$ for each value of b_D via the theoretical function $F(\tau) = 0.5c(W_\tilde{\nu}/\tilde{\nu})/b_D$ (Spitzer 1978), the column density of ^{12}CO at level

J'' is

$$N_{J''}(^{12}\mathrm{CO}) = \zeta \left(\frac{^{12}\mathrm{C}}{^{13}\mathrm{C}}\right) N_{J''}(^{13}\mathrm{CO}). \quad (4)$$

The ratio between the isotopologues, ^{12}CO/^{13}CO, $\zeta(^{12}\mathrm{C}/^{13}\mathrm{C})$, is an adjustable parameter. In Fig. 6, the ^{13}CO data lie on the linear part of the curves, therefore the lines are optically thin, whereas the ^{12}CO lines lie on the saturated part of the curve and are therefore optically thick.

The best-fitting parameters were found by minimizing the difference between the data and the empirical curve (least squares). First, the $\zeta(^{12}\mathrm{C}/^{13}\mathrm{C})$ parameter was varied. Varying ζ will only move the ^{12}CO points left or right in the curve-of-growth diagram. For each ζ value, χ^2 values between the observed EWs and the synthetic curves were determined by varying b_D. The determination of $\zeta(^{12}\mathrm{C}/^{13}\mathrm{C})$ and b_D is independent on the actual CO column density and excitation. The best fits were obtained for $\zeta(^{12}\mathrm{C}/^{13}\mathrm{C}) = 67 \pm 3$ (1σ) and $b_\mathrm{D} = 11 \pm 1.5\,\mathrm{km\,s^{-1}}$ (1σ). Since the EWs derived from ISAAC are strictly lower limits, we should consider that $\zeta = 67$ is also a lower limit. The errors were determined from the χ^2 surface. The $\zeta(^{12}\mathrm{C}/^{13}\mathrm{C})$ value derived here is an average between the ζ value in the warm wind and that in the cold foreground cloud. The CRIRES spectra show that the main-component profile is a combination of multiple Gaussians. The ζ value of each individual velocity components can be derived using CRIRES data in future studies. The average value of $\zeta(^{12}\mathrm{C}/^{13}\mathrm{C})$ of 67 ± 3 is close to the local interstellar value of 65–77 (e.g. Wilson & Rood 1994; Bensch et al. 2001; Sheffer et al. 2007).

4.2 Rotational diagram

4.2.1 Main component

We used the optically thin ^{13}CO data to construct the rotational diagram based on the ISAAC data that is shown in Fig. 7 for the main component. In a rotational diagram for R-branch absorption lines, the natural logarithm of the lower level column density of a transition $J' \leftarrow J''$ divided by the degeneracy $(2J'' + 1)$, $\log[N_{J''}/(2J'' + 1)]$ is plotted against the lower level energy $E_{J''}/k$ (in K). If the level population is thermalized, at local thermodynamic equilibrium (LTE), the column density at a given level J'' is expressed as

$$N_{J''} = N(\mathrm{CO})(2J'' + 1)\frac{\exp(-E_{J''}/T_\mathrm{kin})}{Q(T_\mathrm{kin})}, \quad (5)$$

where N(CO) is the column density of CO, $E_{J''}$ is the energy of the J''th rotational level expressed in K, $Q(T_\mathrm{kin}) \simeq kT_\mathrm{kin}/B_0 + 1/3$ is a good approximation of the partition function at the gas temperature T_kin (equals to the gas excitation temperature at high temperatures and densities), and B_0 is the rotational constant with $B_0/k = 2.765$ and 2.644 K for ^{12}CO and ^{13}CO, respectively. The data points in a rotational diagram can be fitted by a straight line for an isothermal medium at LTE. The gas temperature is then given by the negative of the inverse of the slope of the line. However, fits with a single-temperature gas to the observed values provide bad results (Fig. 7). Possible non-LTE population was checked using the simple analytical results of McKee et al. (1982). High-J levels in a gas at non-LTE are underpopulated compared to a gas at LTE, which is not seen in our data. Instead, the data are best fitted with the combination of a cold and hot gas at LTE, similar to most YSOs, where CO fundamental absorption lines have been observed. The low-J absorption lines are formed in a cold region [$T_\mathrm{gas} = 45$ K, $N(^{13}\mathrm{CO}) \simeq 3.3 \times 10^{16}\,\mathrm{cm^{-2}}$, $N(^{12}\mathrm{CO}) = 67 \times N(^{13}\mathrm{CO}) \simeq 2.2 \times 10^{18}\,\mathrm{cm^{-2}}$] while the high-$J$ lines ($J \geq 10$) are formed in warm gas [$T_\mathrm{gas} = 753$ K, $N(^{13}\mathrm{CO}) \simeq 10^{17}\,\mathrm{cm^{-2}}$, $N(^{12}\mathrm{CO}) \simeq 6.7 \times 10^{18}\,\mathrm{cm^{-2}}$]. The results are summarized in Table 3. The LTE level population and the non-detection of high-velocity gas in emission in the millimetre indicate that the warm component arises in a low surface area and high density region ($n_\mathrm{H} > 10^7\,\mathrm{cm^{-3}}$) with a very small filling factor in the millimetre.

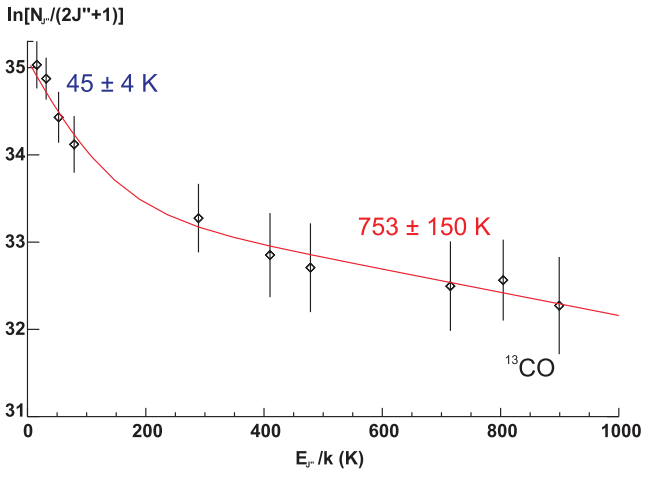

Figure 7. Rotational diagram of ^{13}CO for the main component. The fit by the two-slab model is overplotted.

4.2.2 High-velocity gas

The blue absorption component in the ISAAC data was assumed optically thin, because the wing is absent in ^{13}CO, as testified by the ^{12}CO and ^{13}CO profiles in Fig. 3. We constructed a rotational diagram, displayed in Fig. 8, taking into account the transitions from levels detected in the R branch and $b_\mathrm{D} = 11\,\mathrm{km\,s^{-1}}$ to correct for optical thicknesses. Two gas components have been fitted to the data. Warm gas at $\sim 116^{+53}_{-28}$ K with column density of $2.0^{+1.7}_{-0.9} \times 10^{17}\,\mathrm{cm^{-2}}$ and hot gas at $\sim 1338^{+2298}_{-518}$ K with column density of $3.3^{+5.4}_{-1.2} \times 10^{17}\,\mathrm{cm^{-1}}$ provide the best fit (Table 3). The total column density of high-velocity gas is a factor of 10 smaller than that of the main absorbing gas using ^{12}CO, assuming that the ^{12}CO lines are optically thin.

4.2.3 CRIRES components

We drew the rotational diagram for ^{12}CO for the individual substructures in Fig. 9 and the results are summarized in the lower part of Table 3. The CRIRES lines probe the cool gas towards LLN 19 with substructure temperatures ranging from 47 to 396 K.

High-J ^{13}CO transitions up to $R(22)$ were available in the ISAAC data set to constrain the high-temperature gas component but they were not observed with CRIRES. The lack of high-temperature gas tracers explains the lower overall gas temperature derived from the CRIRES data. Optically thick ^{12}CO lines were used to derive the column densities with the optical depth corrections that were applied to the blue-wing ISAAC data ($b_\mathrm{D} = 11\,\mathrm{km\,s^{-1}}$). The total column density for the main component, which comprises the components at +9, −11.5 and −27 km s^{-1}, is $7.3 \times 10^{17}\,\mathrm{cm^{-2}}$, a factor $\sim$10 lower than the value derived from the ^{13}CO ISAAC data. The column density of the component at $-27\,\mathrm{km\,s^{-1}}$ is uncertain by a

Table 3. Column densities and temperatures derived from the rotational diagram analysis. The upper part of the table corresponds to the parameters derived using the ISAAC data, while the lower part of the table corresponds to the parameters derived using the CRIRES data. The formal errors are 1σ from the least-squares fits. The ^{12}CO column densities of the cold and warm components are derived using the optically thin ^{13}CO data, while the column densities in the blue wing were derived using the ^{12}CO data. The fits to the wing data are poor, which explains the large errors in the derived temperatures and column densities. The column densities derived from the CRIRES EWs are corrected for optical depth effects.

Component	T (K)	$N(^{12}\mathrm{CO})$ (cm^{-2})	$N(^{13}\mathrm{CO})$ (cm^{-2})
		ISAAC data	
Cold main	45 ± 4	$(2.2 \pm 0.6) \times 10^{18}$ [a]	$(3.3 \pm 0.1) \times 10^{16}$
Warm main	753 ± 150	$(6.7 \pm 0.6) \times 10^{18}$ [a]	$(1.0 \pm 0.1) \times 10^{17}$
Cold blue wing	116^{+53}_{-28}	$2.0^{+1.7}_{-0.9} \times 10^{17}$	–
Warm blue wing	1338^{+2298}_{-518}	$3.3^{+5.4}_{-1.2} \times 10^{17}$	–
		CRIRES data	
at $+9\,\mathrm{km\,s^{-1}}$	54^{+9}_{-7}	$1.4^{+1.3}_{-0.8} \times 10^{17}$	–
at $-11.5\,\mathrm{km\,s^{-1}}$	214^{+33}_{-24}	$5.2^{+1.8}_{-1.2} \times 10^{17}$	–
at $-27\,\mathrm{km\,s^{-1}}$	397^{+1050}_{-192}	$6.9^{+183}_{-4.3} \times 10^{16}$	–
at $-43.5\,\mathrm{km\,s^{-1}}$	291^{+66}_{-46}	$4.7^{+2.1}_{-1.3} \times 10^{17}$	–
at $-70\,\mathrm{km\,s^{-1}}$	387^{+128}_{-77}	$1.9^{+0.7}_{-1.1} \times 10^{17}$	–

[a] From ^{13}CO using $^{12}\mathrm{CO}/^{13}\mathrm{CO} = 67$.

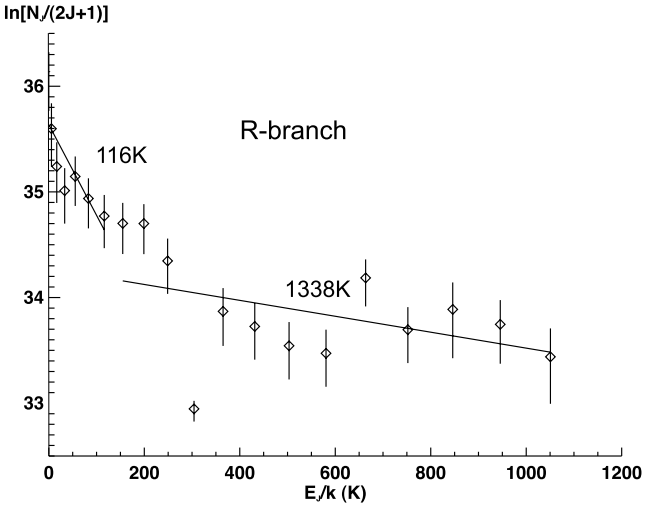

Figure 8. Rotational diagram of the blue-wing component of ^{12}CO.

factor ∼25. The column densities derived from CRIRES data have large systematic errors because of the assumptions made for the optical depth corrections (the Doppler width b_D and the number of absorption features). In the ISAAC data set, the column density of the main component is dominated by the column density of warm gas. Unfortunately, the warm gas cannot be probed in the CRIRES data set, which is limited to transitions up to $P(13)$ (see Fig. 2). The systematic errors and the lack of high-J lines in the CRIRES data set may explain the discrepancy in ^{12}CO column densities derived from the two data sets. The two velocity components at -43 and $-70\,\mathrm{km\,s^{-1}}$ in the CRIRES data match the ISAAC blue-wing component well in terms of temperature (∼290–390 K) and column density (1.9–4.7) $\times\ 10^{17}\,\mathrm{cm}^{-2}$. The reason for the similarity may stem from the fact that the blue-wing parameters were both derived from optically thick ^{12}CO data.

5 WIND MODEL

In this section, we focus on the model fitting on the ISAAC data since they are more complete in the rotational level coverage than the CRIRES data. We used the velocity structure seen in the CRIRES data however to bound the parameters.

5.1 Model description and fitting

The temperature and column density of the high-velocity gas suggest that the absorbing gas may be located in the mixing layer between the outflow and the envelope. The simple analysis of the ISAAC data has assumed an arbitrary distinction between a main component and a blueshifted one. The CRIRES data have shown that the outflow rate of gas is not continuous but may instead proceed by episodes of strong mass-losses. However, a simple static model like the one we adopt here cannot handle dynamical effects, although the model can still give an average value for the mass-loss rate.

We fitted the ^{12}CO and ^{13}CO synthetic transmission spectrum of a wind model to the transmission spectrum of LLN 19. The model focuses on the molecular part of the outflow only.

The spherical wind component of the model is a simplified version of the parametric model of Chandler, Carlstrom & Scoville (1995). The wind is divided into concentric shells located at distances R from the star. The wind is launched from R_in and the size of the spherical wind is R_out. We assume an accelerated wind with velocity of the form:

$$V_w = \left(V_\mathrm{max} - V_{R_\mathrm{in}}\right)\left(1 - \frac{R_\mathrm{in}}{R}\right)^q + V_{R_\mathrm{in}}, \quad (6)$$

where V_{R_in} is the wind velocity at R_in and V_max is the asymptotic wind velocity. The index q controls the variation of the wind velocity with R. The wind velocity does not vary with time in our model.

Assuming a constant mass-loss rate $\dot{m}$ (in $\mathrm{M}_\odot\ \mathrm{yr}^{-1}$) throughout the wind, the spherical wind velocity, mass-loss rate and column density are related by the mass conservation equation

$$n(^{12}\mathrm{CO}) = \frac{\dot{m}}{4\pi m_{\mathrm{H}_2} R^2 V_w (1 - \cos\phi)}\left[\frac{n(^{12}\mathrm{CO})}{n(\mathrm{H}_2)}\right], \quad (7)$$

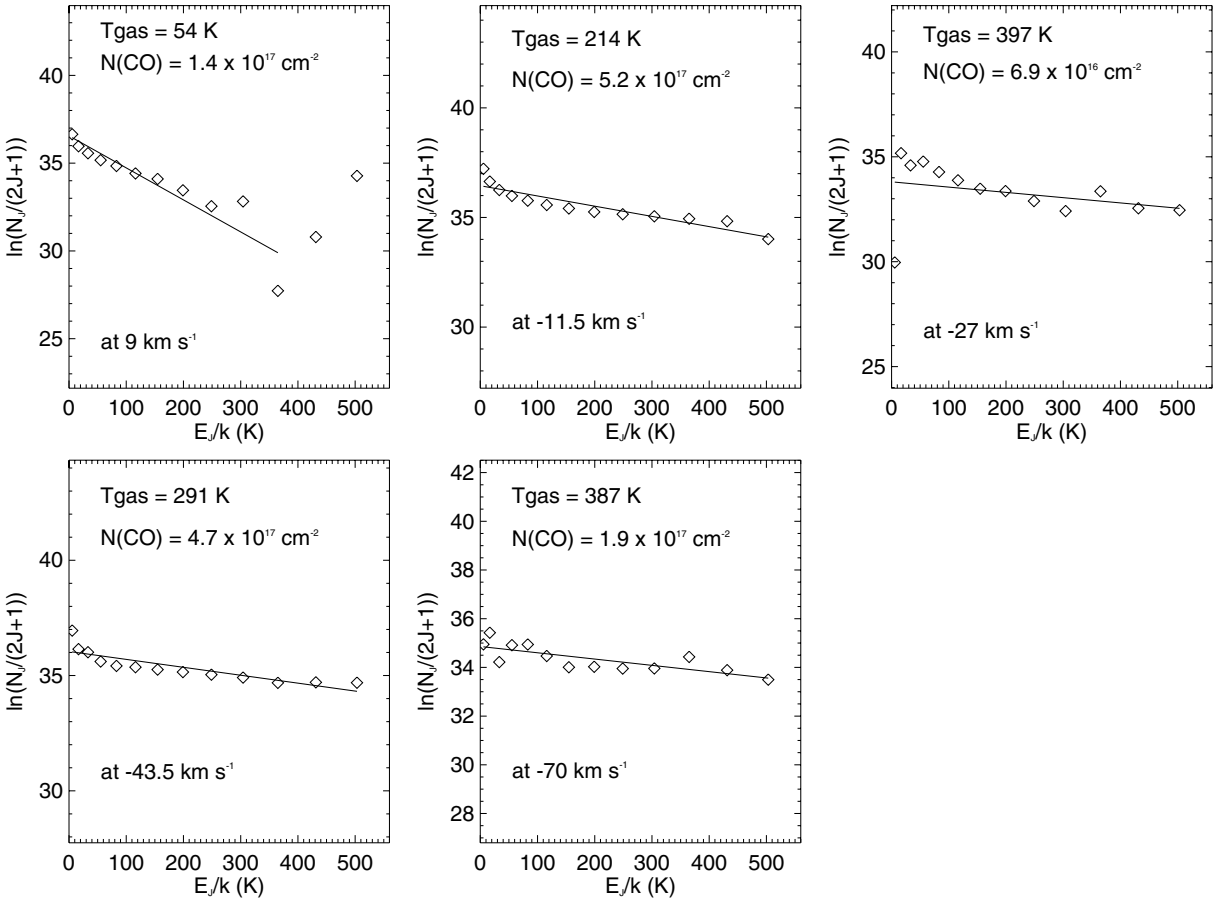

Figure 9. Rotational diagram of ^{12}CO for each substructure components in the CRIRES data. EWs for $P(12)$ and $P(13)$ were not used in the analysis of the 9 km s^{-1} substructure because the absorption features are compromised by strong telluric absorption (see Fig. 2).

where $m_{\rm H_2}$ is the gas molecular mass ($m_{\rm H_2} = 2.2$ amu), $n(^{12}{\rm CO})/n({\rm H_2})$ is the ^{12}CO abundance relative to H_2 and ϕ is the semi-opening angle of the wind (for a spherical wind, $\phi = \pi/2$). For a spherical wind, a shell of thickness ΔR has a column density $\Delta N(^{12}{\rm CO})(R) = n(^{12}{\rm CO})(R) \times \Delta R$ and $\phi = \pi/2$. We assumed that the wind is fully molecular and that $n(^{12}{\rm CO})/n({\rm H_2}) = 10^{-4}$.

The gas temperature was not computed self-consistently, instead we adopted a power law $T_{\rm rot} = T_{\rm in}(R/R_{\rm in})^{-p}$. The gas temperature power-law index can take positive and negative values. If the wind cools radiatively and adiabatically by expansion, then p is positive. The wind can also be heated by shocks and turbulence. In that case the value for p can be negative. The ^{12}CO and ^{13}CO level population are at LTE.

Spectra were computed by a simple line+continuum ray-tracing with $T_{\rm gas} = T_{\rm dust} = T_{\rm rot} = T_{\rm vib}$. The ray-tracing integrates the radiative transfer equation from shell $i-1$ to shell i for one ray taking into account dust (Draine & Lee 1984) and CO gas opacities (Chandra, Maheshwari & Sharma 1996):

$$I_\nu(i) = I_\nu(i-1){\rm e}^{-\tau_\nu(i)} + B_\nu\left[T(i)\right]\left[1 - {\rm e}^{-\tau_\nu(i)}\right]. \quad (8)$$

We removed a low-order polynomial as continuum to the intensity spectra to obtain synthetic transmission spectra $T_{\rm mod}$.

The number of free parameters amounts to eight: $\theta = [R_{\rm in}, R_{\rm out}, V_{R_{\rm in}}, V_{\rm max}, q, \dot{m}, T_{\rm in}, p]$. The intrinsic turbulent line width $b_{\rm D}$ is set to 10 km s^{-1} and the ^{12}CO/^{13}CO ratio is assumed to be 65. The number of data points n is 1020 (1024 minus 2 points at each edge). The number of degrees of freedom (d.o.f.) is thus 1012. The high number of parameters means that degeneracy between parameters is unavoidable. We also imposed physically motivated limits to the parameters. Assuming an outer radius of 100–500 au, we can estimate the mass-loss rate using equation (7), a CO column density of 6.7×10^{18} cm^{-2} and a wind velocity of 50 km s^{-1}. We found that the mass-loss rate is of the order of 10^{-7} M$_\odot$ yr^{-1}. The mass-loss rate ranges from 10^{-8} to 10^{-6} M$_\odot$ yr^{-1} during the fitting procedure. The wind acceleration parameter q was allowed to vary between 0 and 3. The gas temperature can decrease (positive p values) or increase (negative p values) as the wind expands.

We used a non-linear global optimization code based on the SCE algorithm, which mixes evolutionary and simplex algorithm (Duan, Gupta & Sorooshian 1993) to minimize the residual sum squared (RSS) between observational data and model outputs:

$$F(\theta) = {\rm RSS} = \sum_{j=1}^{n}\left[T_{\rm obs}(\tilde{\nu}_j) - T_{\rm mod}(\tilde{\nu}_j, \theta)\right]^2 = \sum_{j=1}^{n} f_j^2(\theta), \quad (9)$$

where $T_{\rm obs}(\tilde{\nu}_j)$ is the observed transmission depth at wavenumber $\tilde{\nu}_j$ and $T_{\rm mod}(\tilde{\nu}_j, \theta)$ is the corresponding modelled transmission with the $k = 11$ parameters. $F(\theta)$ is the RSS or the merit function and is related to the chi-squared. If the noise σ is uniform, by definition $\chi^2_\nu = \chi^2/{\rm d.o.f.} = ({\rm RSS}/\sigma^2)/{\rm d.o.f.}$ Minimizing the RSS is equivalent to minimizing χ^2. We obtained a reduced χ^2_ν of 0.4, which suggests that the noise level is overestimated in average (i.e. the S/N of 99 is underestimated).

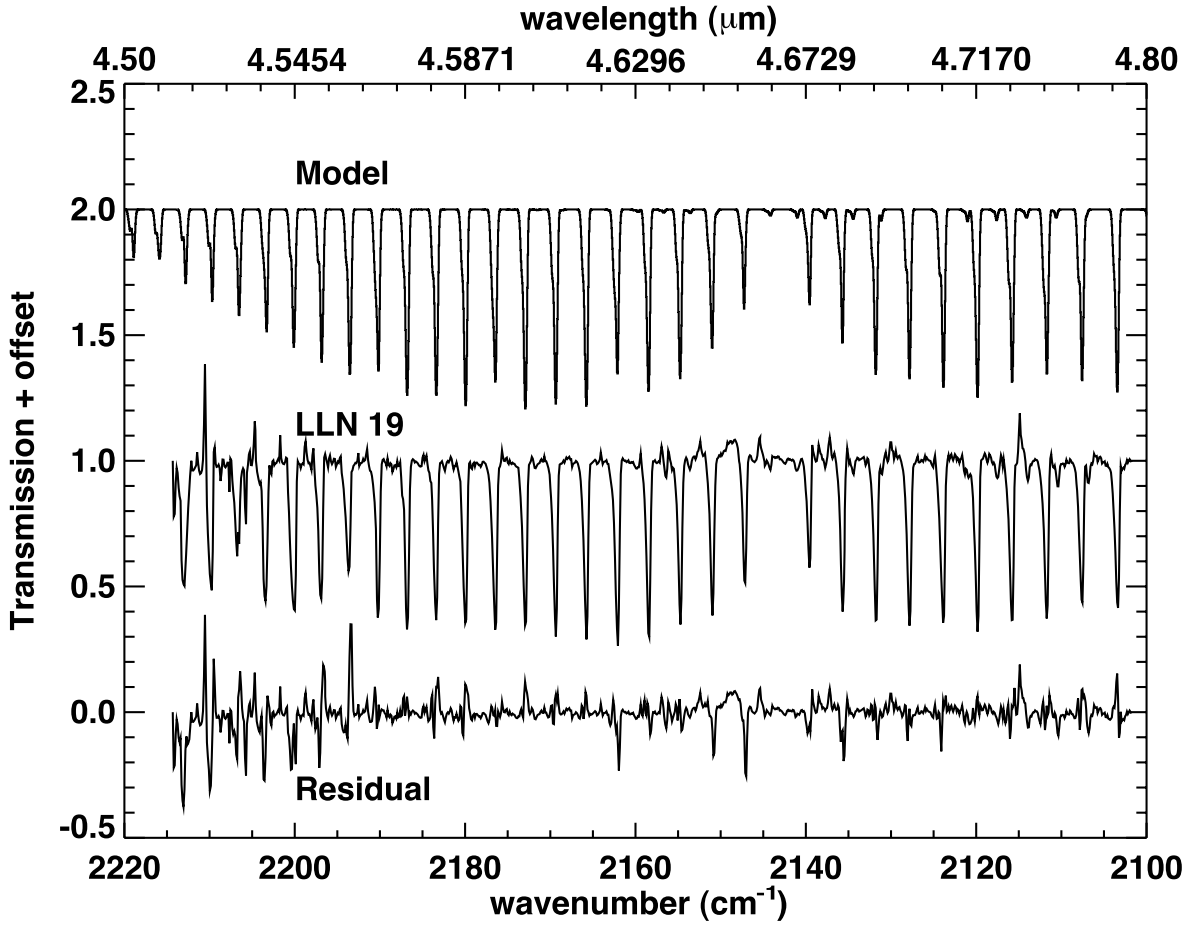

Figure 10. Best fit by the wind model. The upper graph shows the best model synthetic spectrum shifted by +2.0, the middle graph is the observed ISAAC transmission spectrum shifted by +1.0 and the lower graph shows the residual to the best fit. The best fit does not completely account for absorptions of very low- and very high-J transitions.

The SCE is a hybrid algorithm that uses a genetic algorithm with local population evolution replaced by a Nelder–Mead simplex search (Nelder & Mead 1965). The genetic algorithm part ensures that a global minimum can be found, while the Nelder–Mead simplex method provides fast local minimum searches. The SCE method is efficient in finding the global minima of non-linear problems with multilocal minima.

5.2 Model results and error budget

The best synthetic spectrum is compared to the observations in Fig. 10. After subtraction of the observed transmission by the wind model, the residual still show weak absorption in the $J < 3$ lines, testifying of the presence of cold ($T < 100$ K) material, maybe unrelated to LLN 19 where water and CO ice are present. This cold component was analysed in Section 4.1. The fit also fails to explain the relatively noisy high-J absorption lines above $\tilde{\nu} = 2200\,\mathrm{cm}^{-1}$.

For non-linear models, there is no exact way to obtain the covariance matrix for the parameters. Instead, we use the asymptotic approximation and provide the 95 per cent confidence interval (see Appendix for more details). The parameters are relatively well constrained (see Table 4). The asymptotic error method gives unrealistically small errors on the parameters. In addition, we provide the possible range for the parameters where $\chi^2_\nu <$ best $\chi^2_\nu + 1$.

The best-fitting parameters for the wind model are summarized in Table 4. The wind base is at 1 au and reaches 480 au. Infrared absorption measurements do not constrain the spatial extent of the gas along the line of sight. Assuming gas densities greater than $10^6\,\mathrm{cm}^{-3}$ for the CO rotational level population to be at LTE and column density of $5 \times 10^{22}\,\mathrm{cm}^{-2}$, the outflow radius should be smaller than 4500 au, consistent with our derived value. The total ^{12}CO column density in the wind is $3.5 \times 10^{18}\,\mathrm{cm}^{-2}$, lower but comparable to the total of $9.9 \times 10^{18}\,\mathrm{cm}^{-2}$ found using the simple two-slab analysis. The wind temperature is 308 K at the base at 1 au and it stays relatively constant through the warm wind with a slight increase ($p = -0.15$). However, the temperature variation is also consistent with a temperature decrease within the errors.

The asymptotic maximum wind velocity V_{max} is $87\,\mathrm{km\,s}^{-1}$ starting at $16\,\mathrm{km\,s}^{-1}$. The wind velocity index q is 1.1. The mass-loss rate is $4.2 \times 10^{-7}\,\mathrm{M}_\odot\,\mathrm{yr}^{-1}$.

6 WIND-ENVELOPE MODEL

In this section, we attempt to fit the CRIRES data with the same code but with added parameters because the low-J lines indicate that extra material at low velocity is present in the line of sight. In addition to the wind model, we modelled simultaneously the absorption by a quiescent slab component in addition to the wind. The slab of column density N_{env} is at a single temperature T_{env} and

Table 4. Best-fitting parameters to the ISAAC data. No velocity correction has been applied. CI means confidence interval computed from the asymptotic method. The $\chi^2_\nu + 1$ CI is also provided.

	Units	Best-fitting value	95 per cent CI	Best $< (\chi^2_\nu + 1)$ CI	
$R_{\rm in}$	au	1.0	±0.5	0.1	3.9
$R_{\rm out}$	au	480	±99	74	3668
$T_{\rm in}$	K	308	±10	69	925
p		−0.15	±0.26	−0.32	0.40
$V_{R_{\rm in}}$	km s^{-1}	16.1	±0.03	14	19
$V_{\rm max}$	km s^{-1}	87	±3	11	270
q		1.1	±0.3	0.01	2.0
$\dot{m}$	10^{-7} M$_\odot$ yr^{-1}	4.2	±0.7	0.3	11.6
S/N		99			
χ^2_ν		0.4			

moves at velocity $V_{\rm env}$. The widths of the slab and wind absorption lines are 5 and 10 km s^{-1}, respectively, as suggested by the values found in Fig. 4.

We performed two series of fits. In the first series, the wind parameters were bracketed around the best values found by fitting the ISAAC data. In the second series, all parameters were given the freedom to take any physically valid value. The best fit in the first series is plotted in red in Fig. 11 and the best fit in the second series is plotted in green. The parameters for both the fits, the χ^2 of the fits and their asymptotic 95 per cent confidence interval are

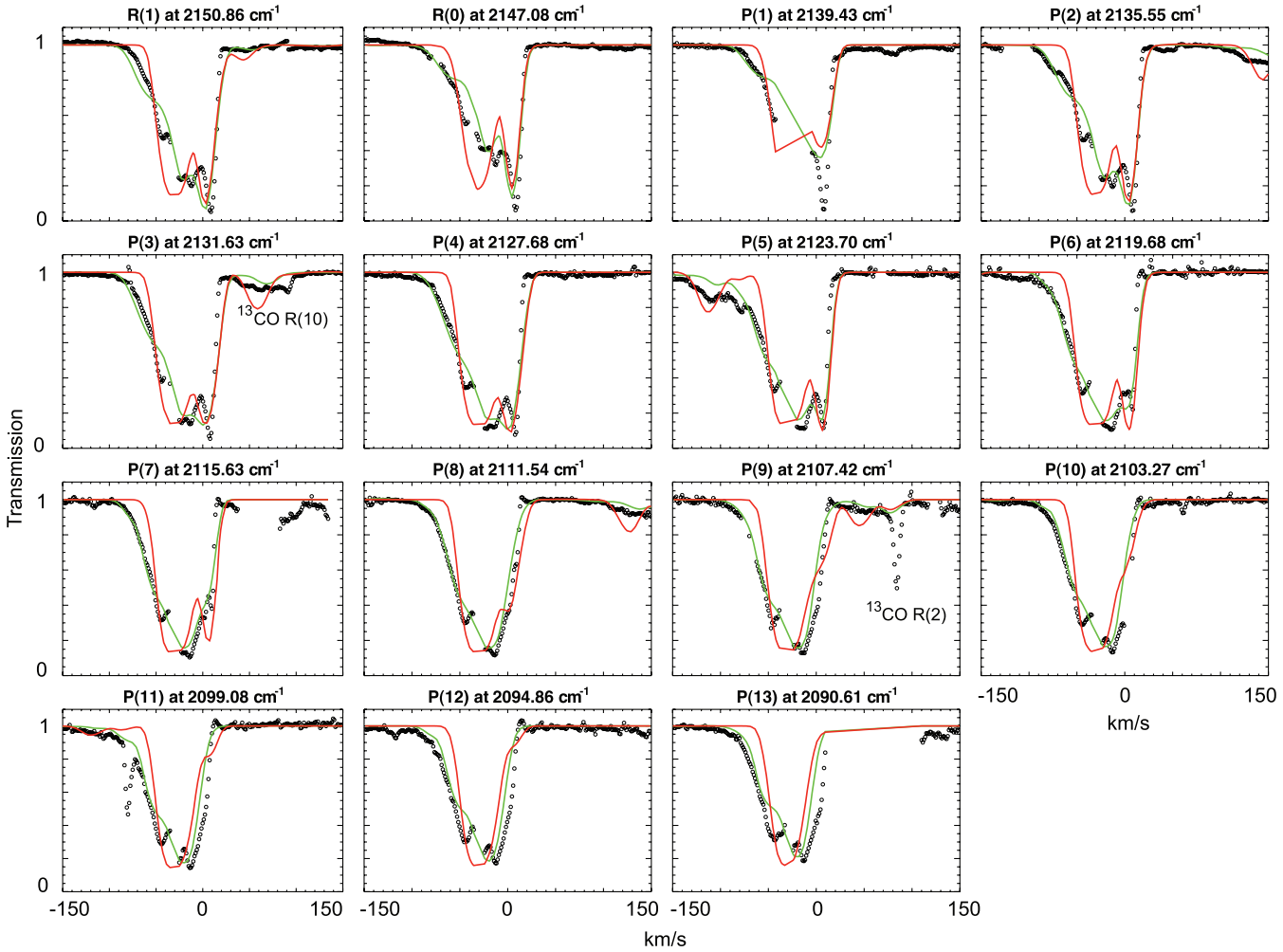

Figure 11. Two fits to the CRIRES observations. The red fit results from a wind+envelope model with mass-loss rate of $\sim 4.2 \times 10^{-7}$ yr^{-1}, while the green fit results from a model with mass-loss rate of $\sim 4.8 \times 10^{-8}$ yr^{-1}. The red fit grossly overestimates the absorption around the −43.5 km s^{-1} features and fails to match the data in the blue tail at ~ -70 km s^{-1}. On the other hand, the green fit underestimates the amount of absorption. Both fits stress the failure of the constant mass-loss rate model.

Table 5. Best-fitting parameters to the CRIRES data for the two series. The confidence intervals (CIs) are approximate statistical errors (see Appendix). Systematic errors are not included.

	Units	Best fit (low $\dot{m}$)	95 per cent CI	Best fit (high $\dot{m}$)	95 per cent CI
$R_{\rm in}$	au	0.14	±0.02	0.9	±2.6
$R_{\rm out}$	au	73	±4	167	−167/+298
$T_{\rm in}$	K	290	±2	340	±6
p		−0.19	±0.08	0.07	±0.8
$V_{R_{\rm in}}$	km s^{-1}	16.0	±0.02	15.9	0.7
$V_{\rm max}$	km s^{-1}	70	±0.6	28	±1
q		2.2	±0.08	2.3	±1.2
$\dot{m}$	10^{-7} M$_\odot$ yr^{-1}	0.48	±0.02	4.2	±3.5
$N_{\rm slab}$	10^{17} cm^{-2}	4.3	±0.015	6.0	±1.8
$T_{\rm slab}$	K	51	±1	83	±3
$V_{\rm slab}$	km s^{-1}	−8.9	±0.03	−8.6	±0.02
χ^2_ν	–	125	–	224	–

summarized in Table 5. We only provide the asymptotic errors as the fits are far from the optimal ($\chi^2_\nu > 100$). Both the fits, which are based on a constant mass-loss rate wind model, fail to reproduce the complex shape of the ^{12}CO absorption profile but the fit with a mass-loss rate an order of magnitude lower than the value found by fitting the ISAAC data seems to give a better match. A closer inspection reveals that both fits struggle in the region between −30 and −50 km s^{-1}. The low mass-loss rate model underpredicts the amount of absorption, whereas the high mass-loss rate model overpredicts the absorption feature. The high mass-loss rate fit overpredicts the amount of absorption while the low mass-loss rate fit underpredicts the amount of material in this velocity range. The mass-loss rates provided by the two fits bracket the mass-loss rates. The temperature of the slab is between 51 and 83 K, warmer than the value derived from the Gaussian-fitting analysis. As expected from the ^{13}CO ISAAC data, the ^{12}CO column density is three orders of magnitude higher, because the rotational diagram analysis vastly underestimates column densities in very optically thick cases. The temperature profile is not well constrained. Both, a slightly increase or decreasing temperature profile, are consistent with the data.

7 DISCUSSION

7.1 Gaseous and solid CO around LLN 19?

From our analysis of the gas- and solid-phase CO, the $N_{\rm ice}({\rm CO})/N_{\rm gas}({\rm CO})$ ratio is $\simeq 5 \times 10^{-3}$. The CO ice/gas is lowest seen towards other YSOs in the Vela molecular cloud with similar bolometric luminosity ($L_* = 1600\,{\rm L}_\odot$ for LLN 19) but close to the value derived in a few high-mass YSOs ($L_*/{\rm L}_\odot > 10^4$), which have less than 1 per cent of CO in the solid state (Mitchell et al. 1990). Other high-mass YSOs have much higher fraction of CO in the solid state (i.e. 22.7 per cent CO ice in the envelope of RAFGL 7009S (Dartois et al. 1998)). Also, contrary to other YSOs in the Vela cloud, LLN 19 has a low water ice abundance with respect to H_2 of 1.1×10^{-5} and a total water column density of $N_{\rm ice}({\rm H_2O}) = 1.05 \pm 0.2 \times 10^{18}$ cm^{-2} (Thi et al. 2006). One explanation is that LLN 19 is in a more evolved stage than the other YSOs studied in Thi et al. (2006) and has already cleared its surrounding envelope via powerful outflows. In this case, both water and CO ices are most likely located in the foreground material along the line of sight towards LLN 19.

Another way to constrain the amount of gas-phase CO depletion is to compare the estimated total column density CO molecules in the line of sight from extinction studies and the detected amount of CO in the gas phase. The total CO column density in the slab model is 8.9×10^{18} cm^{-2} and 3.5×10^{18} cm^{-2} in the wind model. In comparison, the fit to the 10 μm silicate feature using a 1D radiative transfer code gives $N({\rm CO}) \simeq 8.5 \times 10^{18}$ cm^{-2} (Thi et al. 2006) assuming [H_2]/[CO]=10^4, i.e. without CO depletion. The similarity between the observed and estimated CO column density suggests that CO is lightly frozen on to grain surfaces along the line of sight towards LLN 19.

We can also estimate the total CO column density from the visual extinction. We adopt the conversion factor $N_{\rm H}({\rm CO})/A_{\rm V} \sim 9 \times 10^{16}$ cm^{-2} mag^{-1}, if there is no CO depletion (Frerking, Langer & Wilson 1982). The visual extinction is estimated from the observed $E(H-K)$ with $A_{\rm V} = (15.3 \pm 0.6) \times (H-K)$ (Rieke & Lebofsky 1985). The intrinsic $H-K$ colour of early B up to F stars is close to zero. Assuming that the K-band flux is dominated by the extinct central source, $E(H-K) \simeq H-K$. The H- and K-band magnitudes are 11.92 and 8.88, respectively (Liseau et al. 1992), which translates into an extinction of ∼46 mag. The derived value of $N({\rm CO})$ is 4.2×10^{18} cm^{-2}, smaller but close to the detected total value of 8.9×10^{18} cm^{-2} in the two-slab model and very close to the value of 3.5×10^{18} cm^{-2}, found using the wind model. The observed gas-phase CO column density accounts for the predicted column, indicating that most CO molecules are in the gas phase.

The two different fitting methods agree on the fact that LLN 19 shows a much larger amount of warm than cold gas. The temperature of the cooler component (45 K in the two-slab model, 200–300 K in the wind model) is much higher than the sublimation temperature of the pure CO ice (20 K) and is consistent with the low $N_{\rm ice}({\rm CO})/N_{\rm gas}({\rm CO})$ ratio of $\simeq 5 \times 10^{-3}$. Because LLN 19 is located in a dense stellar cluster environment, its outer envelope may be heated above the CO condensation/sublimation temperature by the ambient radiation field generated by the nearby stars. This phenomenon has been shown to work to explain molecular depletion in envelopes around intermediate-mass YSO (Jørgensen et al. 2006).

Rettig et al. (2006) found higher $N_{\rm gas}({\rm CO})$ than expected from extinction studies of four YSOs and suggest that dust grains are settling in the disc mid-plane. The presence of an outflow may be

considered an indirect evidence for the existence of a circumstellar disc around LLN 19. The high velocity attained by the outflowing gas and the absence of redshifted absorption indicate that the circumstellar disc would be seen at low inclination with respect to the axis of rotation, and the line of sight towards LLN 19 would intercept a small amount of disc material only. However, the extinction in the wind itself ($A_V > 50$) is high enough to mask the redshifted absorption by recessing outflowing gas.

A low CO depletion found in our study concurs with observations of the CS millimetre line by Giannini et al. (2005), which suggest that no molecular depletion occurs in the Vela molecular cloud on a global scale.

7.2 ^{12}CO/^{13}CO ratio

Goto et al. (2003) compared optically thin ^{12}CO $v = 2 \leftarrow 0$ and ^{13}CO $v = 1 \leftarrow 0$ towards three YSOs. They derived a ^{12}CO/^{13}CO ratio of 137 ± 9, 86 ± 49 and 158 towards LkHα 101, AFGL 490 and Mon R2 IRS3, respectively. Scoville et al. (1983) found a ^{12}CO/^{13}CO ratio of ∼100 towards the BN/KL object. The ratios are 1.5–2 times higher than the generally accepted interstellar value. We estimated a ^{12}CO/^{13}CO ratio of 67 ± 3 towards LLN 19, close to the average interstellar value. The line of sights in Goto et al.'s (2003) study probe quiescent (dv = 2–3.5 km s^{-1}) cold foreground clouds, whereas our data suggest that most of the CO gas is located in a turbulent warm region around LLN 19.

More recently, a detail study of CO isotopologues absorption in the *M* band with CRIRES towards the protoplanetary disc VV CrA and the YSO Reipurth 50 gives a value of $\zeta(^{12}C/^{13}C)$ of 100 (Smith et al. 2009). One possible explanation for the higher ratio is selective photodissociation of ^{13}CO in protoplanetary discs and protostellar environment. It appears that the ^{12}CO/^{13}CO ratio may be inhomogeneous within a cloud. This supports the idea that local differentiation processes occur. Detailed analysis of the ^{12}CO/^{13}CO ratio using optically thin $v = 2 \leftarrow 0$ ^{12}CO absorption of the cold component at 9 km s^{-1} will be published elsewhere (Smith et al.). Interestingly, the $\zeta(^{12}C/^{13}C)$ for CO ice has been found to be ∼70 (Boogert, Blake & Tielens 2002b; Pontoppidan et al. 2003), close to the quiescent interstellar gas-phase values (60–80).

7.3 Properties of the outflowing gas

We derived some properties of the outflowing gas in LLN 19 and summarized them in Table 6.

The geometry of absorbing gases cannot be constrained with spatially unresolved observations. The gas may be outflowing in the form of spherical shells or in highly collimated jets. For simplicity, we have assumed that the wind is spherical, purely molecular and that the $n(CO)/n(H_2)$ ratio is 10^{-4}.

LLN 19 has a luminosity of 1600 L$_\odot$. Its inferred mass-loss rate of 4.8 × 10^{-8} to 4.2 × 10^{-7} M$_\odot$ yr^{-1} is two to three orders of magnitude lower than that in mid- to early-B ($L_* > 10^4$ L$_\odot$) YSOs, ∼10^{-5} to a few 10^{-3} M$_\odot$ yr^{-1} (Mitchell et al. 1991; Arce et al. 2007). Low mass-loss rates of the order of 10^{-7} M$_\odot$ yr^{-1} are found for low-mass ($L_* \leq 1$ L$_\odot$) young stars (Bontemps et al. 1996). Our result is marginally consistent with a scaling of the mass-loss rate with luminosity (Nisini et al. 1995).

The source of the momentum carried by extended bipolar outflows remains undetermined. By computing the momentum of the young outflows, we may compare them to values derived from millimetre observations of extended outflows. The assumption of spherical flow in our modelling implies that the derived momenta are lower limits. The momentum per unit area of a shell, assuming a thin shell compared to its radius R, is

$$p_{\rm shell}(R) = \dot{m}\frac{{\rm d}R}{4\pi R^2}, \tag{10}$$

and the momentum at the outer radius $R_{\rm out}$ is

$$P = \int_{R_{\rm in}}^{R_{\rm out}} \dot{m}\,{\rm d}R \simeq \dot{m}R_{\rm out}. \tag{11}$$

The outer radius of the wind from the model is $R_{\rm out} \simeq$ 73–480 au [or (1–7.2) × 10^{15} cm], which is consistent with values found for high-mass stars. The momentum per unit area in the wind at the outer radius is given by (Mitchell et al. 1991):

$$p(R_{\rm out}) = N(CO)\left[\frac{n({\rm H_2})}{n({\rm CO})}\right] m({\rm H_2})V_w = \frac{\dot{m}}{4\pi R_{\rm out}}. \tag{12}$$

We derived a momentum per unit area $p(R_{\rm out})$ of (2.9–8.4) × 10^2 g cm^{-1} s^{-1} and a total momentum P of (0.19–9.6) × 10^{-4} M$_\odot$ km s^{-1}. The momentum per unit area is ∼100 times and the total momentum is also ∼1000 times smaller than in outflows around high-mass YSOs (Mitchell et al. 1991). The momentum rate (also called momentum flux or force) of (0.4–7.9) × 10^{-5} M$_\odot$ km s^{-1} yr^{-1} is also similar to the rates found for outflows from low-mass protostars (Arce et al. 2007).

We also estimated the dynamical time-scale of the wind, which corresponds to the time for a gas shell to reach the wind outer radius $R_{\rm out}$ from $R_{\rm in}$. The mass in a shell at distance R from the source is

$$m_{\rm shell} = {\rm d}m = 4\pi R^2 m_{\rm H_2}{\rm d}N. \tag{13}$$

The constant mass-loss rate can be rewritten as

$$\dot{m} = \frac{{\rm d}m}{{\rm d}t} = 4\pi R^2 m_{\rm H_2}\frac{{\rm d}N(R)}{{\rm d}t} \simeq 4\pi R_{\rm out}^2 m_{\rm H_2}\frac{N(R_{\rm out})}{t_{\rm dyn}}. \tag{14}$$

The dynamical time-scale is thus

$$t_{\rm dyn} \simeq 4\pi R_{\rm out}^2 m_{\rm H_2}\frac{N(R_{\rm out})}{\dot{m}}, \tag{15}$$

Table 6. Outflow parameters.

	Units	ISAAC	CRIRES (low $\dot{m}$)	CRIRES (high $\dot{m}$)
Total column density $N(H_2)$	10^{22} cm^{-2}	3.5	2.2	2.6
Mass-loss rate $\dot{m}$	10^{-7} M$_\odot$ yr^{-1}	4.2	0.48	4.2
Momentum per unit area p	10^2 g cm^{-1} s^{-1}	2.9	2.5	8.4
Total momentum P	M$_\odot$ km s^{-1}	9.6 × 10^{-4}	1.9 × 10^{-5}	3.3 × 10^{-4}
Momentum rate	M$_\odot$ km s^{-1} yr^{-1}	7.9 × 10^{-5}	3.9 × 10^{-6}	1.2 × 10^{-5}
Dynamical time-scale $t_{\rm dyn}$	yr	26	5	28

with $N = 10^4 \times N(^{12}\mathrm{CO}) = 3.5 \times 10^{22}\,\mathrm{cm}^{-2}$ at $R_{\rm out}$. We find that $t_{\rm dyn} \sim 28$ yr at the outer radius. Using the fits to the CRIRES data, we estimate the dynamical time-scale to a range between 5 and 28 yr. Therefore, whatever the actual value, the dynamical time-scale is much shorter than the values derived from extended molecular outflows in the millimetre.

The dynamical time-scale is consistent with the values found for high-mass YSOs (2–200 yr). The total momentum and the dynamical time-scale for the extended outflow obtained by mapping the environment of LLN 19 (8×4 arcmin^2) in ^{12}CO $J = 1 \rightarrow 0$ is $171\,\mathrm{M}_\odot\,\mathrm{km\,s}^{-1}$ and $t_{\rm dyn} \sim 1.6 \times 10^5$ yr, (Wouterloot & Brand 1999). Those values were derived assuming a distance of 2.24 kpc. The discrepancy between the millimetre and infrared values suggests that the CO fundamental lines are probing the recent history (< few 100 yr) of the outflow. Outflows change morphology with time (Arce et al. 2007). The youngest outflows tend to be highly collimated or include a very collimated component while older sources are less collimated with wider opening angles. Finally, the sharp drop in total momentum indicates that the outflow was probably much more active in the past.

The high-resolution CRIRES data confirm the picture drawn from the fitting of the medium-resolution ISAAC data. The substructures seen in the CO absorption lines at different velocities further suggest that the outflow mass-loss is episodic with at least two major events. We bracketed the mass-loss rate between 0.48 and $4.2 \times 10^{-7}\,\mathrm{M}_\odot\,\mathrm{yr}^{-1}$. This is an order of magnitude variation in mass-loss and can be achieved in the context of FU Orionis-type burst (e.g. Calvet, Hartmann & Kenyon 1993). Multiple blueshifted absorptions are also found in high-mass YSOs and are attributed to episodic mass-loss events (Mitchell et al. 1991).

Fig. 12 summarizes schematically the four major outflow models. From all the four models, only the jet-bow shock model predicts episodic variation in jet properties as observed towards LLN 19 (Arce et al. 2007). Also the jet-bow shock model is the sole model that can explain a temperature and velocity increase with distance from the outflow source.

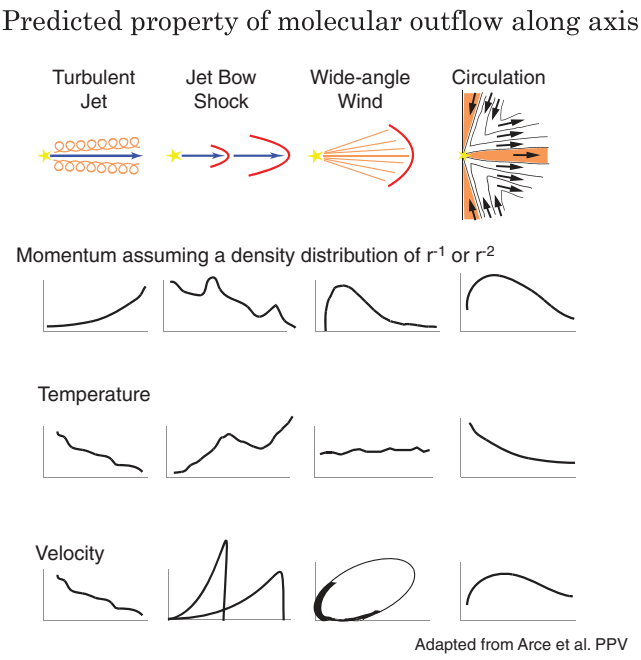

Figure 12. Schematics showing different outflow models. The outflow momentum, temperature and velocity profile along the axis are shown for the four major types of models: turbulent jet, jet bow shock, wide-angle wind and circulation. The schematics are adapted from Arce et al. (2007).

Another peculiar feature of the CO lines towards LLN 19 is the intrinsic line widths. Generally, ^{12}CO ro-vibrational absorptions/emissions towards YSOs are dominated by a hot component at $T_{\rm gas} > 600$ K (e.g. Mitchell et al. 1990). The intrinsic width is low 3–5 km s^{-1} in contrast to our result (dv = 10–12 km s^{-1}) for the outflowing gas, although widths up to 8–10 km s^{-1} have been observed. Narrow cold gas found in the line of sight of high-mass YSOs is attributed to gas in the extended envelope. The wind model-envelope fit to the CRIRES data also suggests that a cold envelope may be present in the line of sight.

One possibility for the warm gas to show large intrinsic width is that turbulence is at play. The detection of turbulent gas would be tantalising. The decay of turbulent eddies could provide the necessary heating to keep large amount of gas at ∼100–1000 K as the radiative heating from the central star decreases with distances. One possible origin for the turbulence are Kelvin–Helmholtz instabilities caused by the interaction of atomic jet-entraining molecular material (Delamater, Frank & Hartmann 2003).

Conversely, the jet-bow shock model of outflows provides a scenario to generate turbulent gases (see Fig. 12). The atomic jets from the inner disc surfaces impact the ambient gas creating shocks. In turn, the high-pressure gas between the shocks is ejected sideways. This high-pressure gas interacts with unperturbed molecular gas, generating turbulences. Shocks will heat the gas to several hundred kelvin, consistent with the gas temperatures of the different substructures. The jet bow model can explain the slight increase of gas temperature with radius contrary to the turbulent jet model. However the 95 per cent confidence interval for the gas temperature allows decreasing gas temperature with distance to the star (Table 4). A flat temperature profile would be consistent with the wide-angle wind model. The large uncertainties in the model parameters, especially for the gas temperature profile, prevent us to favour a specific outflow model.

8 CONCLUSIONS

We analysed medium ($R \sim 10\,000$) and high-resolution ($R \sim 100\,000$) 4.5–4.8 μm spectra of the embedded intermediate-mass YSO LLN 19 in the Vela molecular cloud. Gas-phase ^{12}CO and ^{13}CO ro-vibrational lines have been analysed with a curve of growth and a rotational diagram, and also fitted with by a wind model. Both analyses give similar values for the total column density of warm CO gas and a ^{12}C/^{13}C isotopic ratio of 67 ± 3, lower than values close to 100 found in other studies using infrared absorption lines. The discrepancy in ^{12}C/^{13}C isotopic ratios derived from CO may just reflect the occurrence of varied chemical phenomena in molecular clouds and star-forming regions.

The CO gas towards LLN 19 arises from an outflowing warm gas. Most CO molecules are in the gas phase with less than 0.5 per cent condensed on grain surfaces, maybe in a foreground cloud. The wind parameters of LLN 19 are closer to those from low-mass protostars than high-mass protostars, as seen in infrared absorption. The warm outflowing gas has been created only recently with a dynamical time-scale of less than 28 yr, if the data are analysed in the context of a static spherical wide-angle wind model. However, the kinematics of the outflow as seen in the high spectral resolution CRIRES data are more consistent with an episodic jet-bow shock

model, where the internal bow shocks lead to high pressure and high temperature shells. A dynamical mass-loss rate model is warranted.

LLN 19 (IRAS 08470−4321) is a good example of an object in the phase of cleaning its envelope by an outflow. Temporal monitoring of LLN 19 with CRIRES would provide further clues on the evolution of its outflow.

ACKNOWLEDGMENTS

WFT is supported by a Scottish Universities Physics Alliance (SUPA) fellowship in astrobiology. This research is supported by the Netherlands Research School for Astronomy (NOVA) and a NWO Spinoza grant. KMP acknowledges a Hubble fellowship. The authors wish to thank the VLT staff for all their help in obtaining the observations. WFT thanks Peder Noberg for discussions on statistics and data fitting. We thank the referee for his/her useful comments and suggestions.

REFERENCES

Arce H. G., Goodman A. A., 2001, ApJ, 554, 132
Arce H. G., Shepherd D., Gueth F., Lee C.-F., Bachiller R., Rosen A., Beuther H., 2007, in Reipurth B., Jewitt D., Keil K., eds, Protostars and Planets V. Univ. Arizona Press, Tucson, pp 245–260
Bensch F., Pak I., Wouterloot J. G. A., Klapper G., Winnewisser G., 2001, ApJ, 562, L185
Bik A., Thi W. F., 2004, A&A, 427, L13
Bontemps S., Andre P., Terebey S., Cabrit S., 1996, A&A, 311, 858
Boogert A. C. A., Hogerheijde M. R., Blake G. A., 2002a, ApJ, 568, 761
Boogert A. C. A., Blake G. A., Tielens A. G. G. M., 2002b, ApJ, 577, 271
Boogert A. C. A., Blake G. A., Öberg K., 2004, ApJ, 615, 344
Brittain S. D., Simon T., Najita J. R., Rettig T. W., 2007, ApJ, 659, 685
Calvet N., Hartmann L., Kenyon S. J., 1993, ApJ, 402, 623
Carmona A., van den Ancker M. E., Thi W.-F., Goto M., Henning T., 2005, A&A, 436, 977
Chandler C. J., Carlstrom J. E., Scoville N. Z., 1995, ApJ, 446, 793
Chandra S., Maheshwari V. U., Sharma A. K., 1996, A&AS, 117, 557
Dartois E., D'Hendecourt L., Boulanger F., Jourdain de Muizon M., Breitfellner M., Puget J., Habing H. J., 1998, A&A, 331, 651
Delamater G., Frank A., Hartmann L., 2003, ApJ, 530, 923
Donaldson J. R., Schnabel R. B., 1987, Technometrics, 29, 69
Draine B. T., Lee H. M., 1984, ApJ, 285, 89
Duan Q. Y., Gupta V. K., Sorooshian S., 1993, J. Optimiz. Theor. Appl., 76, 501
Evans N. J., II, Lacy J. H., Carr J. S., 1991, ApJ, 383, 674
Frerking M. A., Langer W. D., Wilson R. W., 1982, ApJ, 262, 590
Gerakines P. A., Schutte W. A., Greenberg J. M., van Dishoeck E. F., 1995, A&A, 296, 810
Giannini T. et al., 2005, A&A, 433, 941
Goorvitch D., Chackerian C., 1994, ApJS, 91, 483
Goto M. et al., 2003, ApJ, 598, 1038
Jiang G. J., Person W. B., Brown K. G., 1975, J. Chem. Phys., 62, 1201
Jørgensen J. K., Johnstone D., van Dishoeck E. F., Doty S. D., 2006, A&A, 449, 609
Knez C., Lacy J. H., Evans N. J., van Dishoeck E. F., Richter M. J., 2009, ApJ, 696, 471
Lahuis F. et al., 2006, ApJ, 636, L145
Liseau R., Lorenzetti D., Nisini B., Spinoglio L., Moneti A., 1992, A&A, 265, 577
Lorenzetti D., Giannini T., Vitali F., Massi F., Nisini B., 2002, ApJ, 564, 839
McKee C. F., Storey J. W. V., Watson D. M., Green S., 1982, ApJ, 259, 647
Massi F., Giannini T., Lorenzetti D., Liseau R., Moneti A., Andreani P., 1999, A&AS, 136, 471
Mitchell G. F., Maillard J., Allen M., Beer R., Belcourt K., 1990, ApJ, 363, 554
Mitchell G. F., Maillard J.-P., Hasegawa T. I., 1991, ApJ, 371, 342
Nelder J. A., Mead R., 1965, Computer Journal, 7, 308
Nisini B., Milillo A., Saraceno P., Vitali F., 1995, A&A, 302, 169
Palla F., Stahler S. W., 1993, ApJ, 418, 414
Pontoppidan K., van Dishoeck E., 2005, in Käufl H. U., Siebenmorgen R., Moorwood A. F. M., eds, ESO Astrophys. Symp. Vol. XX, High Resolution Infrared Spectroscopy in Astronomy. Springer, Berlin, p. 168
Pontoppidan K. M., Schöier F. L., van Dishoeck E. F., Dartois E., 2002, A&A, 393, 585
Pontoppidan K. M. et al., 2003, A&A, 408, 981
Pontoppidan K. M., Blake G. A., van Dishoeck E. F., Smette A., Ireland M. J., Brown J., 2008, ApJ, 684, 1323
Rettig T., Brittain S., Simon T., Gibb E., Balsara D. S., Tilley D. A., Kulesa G., 2006, ApJ, 646, 342
Rieke G. H., Lebofsky M. J., 1985, ApJ, 288, 618
Roueff E., Dartois E., Geballe T. R., Gerin M., 2006, A&A, 447, 963
Schmitt B., Greenberg J. M., Grim R. J. A., 1989, ApJ, 340, L33
Scoville N., Kleinmann S. G., Hall D. N. B., Ridgway S. T., 1983, ApJ, 275, 201
Sheffer Y., Rogers M., Federman S. R., Lambert D. L., Gredel R., 2007, ApJ, 667, 1002
Smith R. L., Pontoppidan K. M., Young E. D., Morris M. R., van Dishoeck E. F., 2009, ApJ, 701, 163
Spitzer L., 1978, Physical Processes in the Interstellar Medium. Wiley Inter-Science, New York, p. 333
Stahler S. W., Palla F., 2005, The Formation of Stars. Wiley-VCH, Weinheim, p. 865
Thi W.-F., van Dalen B., Bik A., Waters L. B. F. M., 2005, A&A, 430, L61
Thi W.-F., van Dishoeck E. F., Dartois E., Pontoppidan K. M., Schutte W. A., Ehrenfreund P., d'Hendecourt L., Fraser H. J., 2006, A&A, 449, 251
van Dishoeck E. F.et al., 2003, Messenger, 113, 49
Wall J. V., Jenkins C. R., 2003, Practical Statistics for Astronomers. Cambridge Univ. Press, Cambridge
Wilson T. L., Rood R., 1994, ARA&A, 32, 191
Wouterloot J. G. A., Brand J., 1999, A&AS, 140, 177

APPENDIX A

For non-linear models, there is no exact way to obtain the covariance matrix for the parameters. Nor do the optimization codes give directly error parameters. Parameter confidence intervals are approximated from the Hessian matrix of $\tau_{\rm mod}(\theta)$ at the solution $\theta = \hat{\theta}$ (Donaldson & Schnabel 1987; Wall & Jenkins 2003):

$$H(\hat{\theta}) = 2J(\hat{\theta})^T J(\hat{\theta}) + 2\sum_{j=1}^{n} f_j(\hat{\theta}) H_j(\hat{\theta}), \tag{A1}$$

where $J(\hat{\theta})$ is the Jacobian of $\tau_{\rm mod}(\hat{\theta})$. In the neighbourhood of the solution, $||f_j(\hat{\theta})H_j(\hat{\theta})||$ is neglectable compared to $||J(\hat{\theta})^T J(\hat{\theta})||$. Therefore, the Hessian matrix at the minimum for $F(\theta)$ (equal to the RSS) at $\theta = \hat{\theta}$ can be approximated by

$$H(\hat{\theta}) \simeq 2J(\hat{\theta})^T J(\hat{\theta}). \tag{A2}$$

An unbiased estimate of the parameter covariance matrix is

$$C(\hat{\theta}) = 2\frac{F(\hat{\theta})}{\rm d.o.f.} H(\hat{\theta})^{-1} = \frac{F(\hat{\theta})}{\rm d.o.f.}[J(\hat{\theta})^T J(\hat{\theta})]^{-1}, \tag{A3}$$

where $s^2 = F(\hat{\theta})/{\rm d.o.f.}$ is an unbiased approximation of the residual variance σ^2 ($\sigma \sim s$). The variance of the ith parameter ${\rm var}(\hat{\theta}_i)$ is the ith diagonal element of the matrix $C(\hat{\theta})$. If θ_i^* is the 'true' solution, then the $100(1-\phi)$ percentage confidence interval on $\hat{\theta}_i$ is

$$\hat{\theta}_i - \sqrt{{\rm var}(\hat{\theta}_i)}t_{\rm d.o.f.}^{1-\phi/2} < \theta_i^* < \hat{\theta}_i + \sqrt{{\rm var}(\hat{\theta}_i)}t_{\rm d.o.f.}^{1-\phi/2}, \tag{A4}$$

where $t_{\mathrm{d.o.f.}}^{1-\phi/2}$ is the $100(1-\phi/2)$ percentage point of the two-tail Student t-distribution with d.o.f. degrees of freedom. When the number of degrees of freedom exceeds 150, the Student distribution equals the normal distribution. In our case, a 95 per cent confidence interval would be the parameter $\pm 1.96 \times \sqrt{\mathrm{var}(\hat{\theta}_i)}$. The Jacobian matrix element $J_{ij}(\hat{\theta})$ is approximated by forward finite difference around $\hat{\theta}$

$$J_{ij}(\hat{\theta}) \simeq \frac{\tau_{\mathrm{mod}}(\tilde{\nu}_j, \theta_i) - \tau_{\mathrm{mod}}(\tilde{\nu}_j, \hat{\theta}_i)}{\theta_i - \hat{\theta}_i}. \quad \text{(A5)}$$

In this paper, the parameter intervals are computed for 95 per cent confidence.

This paper has been typeset from a TEX/LATEX file prepared by the author.